NASA Technical Paper 3616

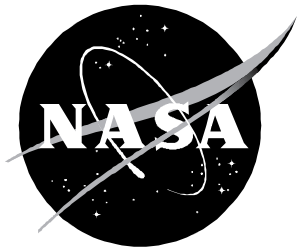

Nonlinear Analysis of the Space Shuttle Superlightweight External Fuel Tank

Michael P. Nemeth, Vicki O. Britt, Timothy J. Collins, and James H. Starnes, Jr.
Langley Research Center • Hampton, Virginia

National Aeronautics and Space Administration
Langley Research Center • Hampton, Virginia 23681-0001

December 1996

Acknowledgments

The authors would like to express their thanks to Richard D. Young, Walter L. Heard, Jr., Charles C. Rankin, Michael Quiggle, and Neil Otte of Lockheed-Martin Engineering and Sciences Services, NASA Langley Research Center (retired), Lockheed-Martin Missiles and Space Company, Lockheed-Martin Manned Space Systems Division, and NASA George C. Marshall Space Flight Center, respectively, for their technical support.

Available electronically at the following URL address: http://techreports.larc.nasa.gov/ltrs/ltrs.html

Printed copies available from the following:

NASA Center for AeroSpace Information
800 Elkridge Landing Road
Linthicum Heights, MD 21090-2934
(301) 621-0390

National Technical Information Service (NTIS)
5285 Port Royal Road
Springfield, VA 22161-2171
(703) 487-4650

Abstract

Results of buckling and nonlinear analyses of the Space Shuttle external tank superlightweight liquid-oxygen (LO_2) tank are presented. Modeling details and results are presented for two prelaunch loading conditions and for two full-scale structural tests that were conducted on the original external tank. The results illustrate three distinctly different types of nonlinear response for thin-walled shells subjected to combined mechanical and thermal loads. The nonlinear response phenomena consist of bifurcation-type buckling, short-wavelength nonlinear bending, and nonlinear collapse associated with a limit point. For each case, the results show that accurate predictions of nonlinear behavior generally require a large-scale, high-fidelity finite-element model. Results are also presented that show that a fluid-filled launch-vehicle shell can be highly sensitive to initial geometric imperfections. In addition, results presented for two full-scale structural tests of the original standard-weight external tank suggest that the finite-element modeling approach used in the present study is sufficient for representing the nonlinear behavior of the superlightweight LO_2 tank.

Introduction

The new era of cooperation in space between the United States and Russia has created a requirement for the Space Shuttle to reach a 51.6° high-inclination orbit. Currently, achieving this orbit requires the payload of the orbiter to be reduced by approximately 10 000 lb. To recover most of the lost payload, National Aeronautics and Space Administration (NASA) is developing a new lightweight external fuel tank for the Space Shuttle made primarily from an aluminum-lithium alloy. This new design, referred to as the superlightweight external tank (SLWT), is expected to weigh approximately 58 000 lb, which is approximately 8000 lb lighter than the lightweight aluminum external tank currently in service.

An important consideration in the design of the SLWT is the nonlinear behavior of the thin-walled regions of the structure that experience compressive stresses. Local or global buckling of the shell wall can cause the thermal protection system (TPS) to separate from the tank, which could cause the vehicle to fail. As part of a plan to ensure that the design does not have a shell-wall instability response, accurate predictions of the nonlinear response of the SLWT are needed. Accurate predictions of the nonlinear response of the SLWT require a large-scale, high-fidelity finite-element model to represent the complex structural details of the SLWT and a robust nonlinear shell analysis capability that can predict local and general instability buckling modes.

One component of the SLWT that experiences significant compressive stresses is the liquid-oxygen (LO_2) tank. A primary goal of this paper is to present results that give an indication of how much additional load, beyond the operational loads for two critical prelaunch loading conditions, the LO_2 tank can withstand before buckling or exhibiting severe bending gradients. Toward that goal, this paper presents results of nonlinear analyses of the LO_2 tank conducted by NASA Langley Research Center personnel for the two prelaunch loading conditions. In addition, results are presented for two full-scale structural tests of the original LO_2 standard-weight tank (SWT) tank configuration, which differs primarily in wall thickness, weight, and material type from the SLWT LO_2 tank. These results demonstrate that the finite-element modeling approach used in the present study yields accurate representations of the nonlinear structural response of the SLWT LO_2 tank.

A second goal is to present results that illustrate some types of nonlinear behavior, and the sensitivity of those behaviors to initial geometric imperfections, that may be encountered in the design of liquid-fuel launch vehicles. Thus, results for the two prelaunch loading conditions and the full-scale structural tests are presented that illustrate three distinctly different types of nonlinear responses of thin-walled shells subjected to combined mechanical and thermal loads. The nonlinear response for the first prelaunch loading condition is characterized by a bifurcation-type buckling response that is insensitive to initial geometric imperfections and exhibits substantial postbuckling load-carrying capacity. In contrast, the nonlinear response for the second prelaunch loading condition is characterized by a short-wavelength bending gradient that grows in amplitude in a stable manner with increasing load. The nonlinear responses for the two full-scale structural tests are characterized by a limit-point response of a doubly curved shell segment that buckles locally. The magnitude of the load corresponding to the limit point is shown to be sensitive to initial geometric imperfections in the LO_2 tank.

For each of the three different nonlinear response phenomena presented, the modeling approach and implementation used to develop a high-fidelity finite-element

model that adequately represents the behavior are discussed. An overview of the SLWT LO_2 tank and intertank structure and loading conditions is presented, the analysis code and finite-element modeling details are discussed, and the results of the linear bifurcation buckling analyses and the nonlinear analyses are presented. Although the modeling approach and implementation presented are for a specific launch vehicle, they represent a general method that can be applied to the design of future liquid-fuel launch vehicles.

SLWT Structure Overview

The Space Shuttle consists of the orbiter, two solid rocket boosters (SRBs), and the external tank (ET), as shown in figure 1. The ET consists of a LO_2 tank, a liquid-hydrogen (LH_2) tank, and an intermediate structure called the intertank (fig. 1). The intertank transmits the weight of the fuel, the ET structural weight, and the orbiter weight to the SRBs prior to launch and transmits thrust loads from the SRBs and the orbiter to the ET during ascent. The SLWT LO_2 tank is a thin-walled monocoque shell made primarily of 2195 aluminum-lithium alloy. The LO_2 tank is approximately 49 ft long and has a maximum diameter of approximately 27.5 ft, as indicated in figure 2. The LO_2 tank consists of a forward ogive section made from 8 gore panels, an aft ogive section made from 12 gore panels, a cylindrical barrel section made from 4 barrel panels, and an aft elliptical dome section made from 12 gore panels. The coordinate systems used to locate the elements of the LO_2 tank and the intertank also are shown in figure 2. The coordinates (*XT, Y, Z*) are typically referred to as the global coordinate system of the ET, and axial positions along the tank are indicated by the coordinate value of *XT* in units of inches. For example, the junction between the forward and aft ogives is indicated by writing *XT* = 536.74 in. Cylindrical coordinates are also used and are given by (r, θ, *XT*), where a positive value of θ is measured from the positive *Z*-axis toward the positive *Y*-axis, as shown in figure 2.

The LO_2 tank also has a forward T-ring and an aft Y-ring frame that support a slosh baffle that prevents the fuel from sloshing during ascent. The slosh baffle, a lightweight (approximately 455 lb), thin-walled structure, is supported by two deep, thin-walled rings at each end that attach to the forward T-ring and the aft Y-ring frame. Other parts of the LO_2 tank include a nonstructural nose cone, a forged forward ogive fitting and cover plate, an aft spherical dome cap that contains the LO_2 suction fitting and a covered manhole, and a vortex baffle attached to the base of the aft dome cap. The LO_2 tank gore and barrel panels are stretch formed, chemically milled, and then welded together. The panels are fabricated with substantial thickness tailoring to reduce structural weight. The panels are made somewhat thicker at the welds to form a stiffener-like region that is used as a weld land. The primary role of the weld lands is to compensate for reduction in shell-wall strength that is caused by welding. Tapering the weld lands in thickness and width along their length reduces weight and alleviates stress concentrations in the shell that result from abrupt changes in thickness.

The intertank is a right-circular cylinder that is made from 2090 and 7075 aluminum alloys and is shown in figure 3. The approximately 22.5-ft-long intertank has a diameter of approximately 27.5 ft and consists of six 45° curved panels that are stiffened longitudinally with external hat stiffeners and are referred to herein as skin-stringer panels. The intertank also has two massive 45° curved panels, referred to as thrust panels, located perpendicular to the *Y*-axis of the intertank (fig. 3) that are stiffened longitudinally with integrally machined external blade stiffeners. These eight panels are assembled into the intertank with mechanical fasteners and are attached to five large internal ring frames, a forward flange, and an aft flange. Longitudinal straps (referred to herein as roll ties) suppress lateral-torsional deflection of the ring frames. The main central ring frame, two thrust panel longerons, and the thrust panels are connected to each end of a tapered beam that is referred to herein as the SRB beam (fig. 3). The SRB beam spans the diameter of the intertank along the *Y*-axis and has a maximum depth (in the *XT* direction) of approximately 43 in. at its midspan. Forged fittings (referred to herein as SRB thrust fittings) that are incapable of transmitting moments are fastened to the ends of the SRB beam. The primary role of the thrust panels is to diffuse the large axial loads introduced by the SRB's into the intertank and then into the LO_2 tank shell wall. The SRB beam compensates for the eccentricity of the concentrated loads introduced by the SRB's. The SRB beam also supports the loads normal to the intertank (parallel to the SRB beam) at the SRB attachment points. The intertank also has a 46-in-high by 52-in-wide frame-reinforced nonstructural access door located along the cylinder generator at approximately $\theta = 146°$.

Critical Prelaunch Loading Conditions

Several critical SLWT loading conditions have been identified by the members of the SWLT team at the NASA George C. Marshall Space Flight Center and at the Lockheed-Martin Manned Space Systems Division. The general characteristics of the critical loads are indicated in figure 4. These loads consist of the wind or aerodynamic pressure loads, the structural weight or inertia, the pressure exerted on the shell wall by the LO_2, the ullage pressure inside the tank, the interface forces exerted by each SRB (indicated by the vectors $\mathbf{R}_1$ and $\mathbf{R}_2$ in fig. 4), the interface forces between the intertank and

the LH_2 tank (indicated by the vectors **F** and **M** in fig. 4), and the thermally induced loads associated with the cryogenic temperatures.

Two critical loading conditions addressed herein correspond to prelanch fueling conditions that occur when the Space Shuttle is on the launch pad. Prior to launch, the LH_2 tank is filled with LH_2, and then the LO_2 tank is filled with LO_2. The first loading condition considered corresponds to a full LH_2 tank and an empty LO_2 tank. For this condition, there is no pressure and no temperature change in the LO_2 tank. However, the lower 45 in. of the intertank are subjected to an axisymmetric uniform through-the-thickness temperature field that varies linearly from −423°F, where the intertank is attached to the LH_2 tank, to 50°F at the top of the LH_2 tank forward dome. The nominal ambient temperature of the LO_2 tank and the intertank prior to fueling is 50°F. The SRB interface forces are given by

$$\mathbf{R}_1 = -224.092\mathbf{i} - 52.223\mathbf{j} - 28.954\mathbf{k} \text{ kips}$$

$$\mathbf{R}_2 = -343.624\mathbf{i} + 48.261\mathbf{j} - 30.754\mathbf{k} \text{ kips}$$

where the vectors $\mathbf{R}_1$ and $\mathbf{R}_2$ are shown in figure 4 and where **i**, **j**, and **k** are standard orthonormal base vectors associated with the *XT*, *Y*, and *Z* axes, respectively. Similarly, the interface force and moment between the intertank and the LH_2 tank are given by

$$\mathbf{F} = 541.593\mathbf{i} + 9.614\mathbf{j} + 63.494\mathbf{k} \text{ kips}$$

$$\mathbf{M} = -310.500\mathbf{i} + 10\,715.745\mathbf{j} + 16\,828.589\mathbf{k} \text{ in-kips}$$

The LO_2 tank is also subjected to wind pressure that has a resultant force given by $-5.652\mathbf{j} - 3.786\mathbf{k}$ kips.

The second prelaunch loading condition considered corresponds to full LH_2 and LO_2 tanks, but without ullage pressure. For this condition, the LO_2 tank is filled to *XT* = 447 in. (fig. 2), which corresponds to a depth of approximately 43 ft. For this case, the hydrostatic pressure distribution in the LO_2 tank is essentially axisymmetric, and the temperature distribution in the LO_2 tank and the intertank is axisymmetric and uniform through the thickness, as shown in figure 5. The specific weight of the LO_2 used in the present study is 0.04123 lb/in^3, and the maximum hydrostatic pressure is approximately 21 psig at the bottom of the tank. The corresponding weight of the LO_2 is approximately 1348 kips.

The temperature field for the LO_2 tank shown in figure 5 has a uniform value of −297°F between *XT* = 447 in. and *XT* = 852.8 in., but varies from a value of −150°F at the nose to −297°F at the free surface of the LO_2 (*XT* = 447 in.). The intertank is subjected to an axisymmetric uniform through-the-thickness temperature field that varies in a piecewise linear manner from −423°F to 50°F and then to −297°F as the intertank is traversed from *XT* = 1129 in. to *XT* = 852.8 in. The temperature field shown in figure 5 represents the changes in the temperature distribution that occur from the nominal prefueling temperature of 50°F.

The SRB interface forces for the second prelaunch loading condition are given by

$$\mathbf{R}_1 = -906.447\mathbf{i} - 105.605\mathbf{j} - 30.502\mathbf{k} \text{ kips}$$

$$\mathbf{R}_2 = -1035.789\mathbf{i} + 108.128\mathbf{j} - 32.557\mathbf{k} \text{ kips}$$

Likewise, the interface force and moment between the intertank and the LH_2 tank are given by

$$\mathbf{F} = 568.113\mathbf{i} + 3.014\mathbf{j} + 66.913\mathbf{k} \text{ kips}$$

$$\mathbf{M} = -354.488\mathbf{i} + 11\,249.318\mathbf{j} + 19\,443.206\mathbf{k} \text{ in-kips}$$

and the LO_2 tank is subjected to a wind load with a resultant force given by $-5.537\mathbf{j} - 3.854\mathbf{k}$ kips.

Analysis Code and Finite-Element Modeling

The results of the linear bifurcation buckling and nonlinear analyses were obtained with the Structural Analysis of General Shells (STAGS) nonlinear structural analysis code for general shells (ref. 1). The finite-element models of the SLWT used in the present study are very complex and include many structural details and the skin thickness variations or tailoring used to reduce structural weight. STAGS was chosen for analyzing the SLWT because of its robust state-of-the-art nonlinear-equation solution algorithms and its general user-input capability that is convenient for modeling branched shells typically used for launch vehicles. In particular, STAGS uses both the full and modified Newton methods to obtain an accurate nonlinear solution, and large rotations in the shell are represented by a corotational algorithm at the element level. The Riks arc-length projection method is used to continue a solution past limit points. STAGS permits complex geometries, loading conditions, and initial geometric imperfections to be modeled in a direct manner by the use of user-written subroutines that are essentially independent of the mesh discretization. For example, these user-written subroutines allow the user to define reference surface geometries; tapered shell walls and stiffener cross sections; and complex nodal force, temperature, and pressure distribution functions in a direct manner, using the FORTRAN computer language. This feature greatly simplified the definition of the finite-element models and the mesh convergence studies conducted in the present study. A description of how the features of STAGS were used in the present study to model the SLWT LO_2 tank and intertank

appears in this section. Details of how the prelaunch loads are simulated are also presented.

In modeling the SLWT LO_2 tank and the intertank, several assumptions were made to simplify the finite-element models. Limited parametric studies were made to determine the adequacy of the assumptions and simplifications. For each case, the modeling assumptions used to simplify the finite-element models were found to be acceptable for analyzing the nonlinear behavior of the SLWT LO_2 tank.

LO_2 Tank Modeling Details

One very useful method for finite-element-mesh generation in STAGS involves defining the number of rows and columns of nodes in a segment of a specific type of shell (reference surface) unit, such as a cylinder, a cone, or a sphere. STAGS includes a library of several different predefined shell units that are based on a specific type of surface parametric representation. For instances where a different surface parametric representation for one of the shell units in the STAGS library is needed, or when a type of shell unit is needed that is not in the STAGS library, the surface information can be input into STAGS with the user-written subroutine called LAME.

For the forward and aft ogive sections of the SLWT LO_2 tank, a parametric representation defined in terms of the global circumferential coordinate θ (defined in fig. 2) and a local axial coordinate of the shell unit were put into LAME. The ogive geometry is based on a nominal 612.0-in. meridional radius of curvature and a 165.5-in. maximum polar radius of curvature. The reference surfaces for the forward ogive fitting and cover plate indicated in figure 2 were input as an ogive segment and a circular segment of a plane, respectively. The ogive segment has an axial (XT) length of 4 in. and polar radii of 25.676 in. and 28.950 in. at XT = 371 in. and XT = 375 in., respectively. Similarly, the flat reference surface of the cover plate has a radius of 25.676 in.

The reference surface for the barrel section of the LO_2 tank was input as a right-circular cone with polar radii equal to 165.359 in. and 165.373 in. at XT = 748.67 in. and XT = 843 in., respectively, and the reference surface for the aft dome section was input as a truncated ellipsoid attached to a smaller spherical cap. To simplify the model, the LO_2 suction fitting and covered manhole were neglected in defining the reference surface (and mesh) of the spherical cap. This simplification is based on the reasoning that the local details of the spherical cap will have a negligible effect on the behavior of the ogives and the barrel. The ellipsoid has a 165.50-in. semimajor axis in the radial direction and a 124.125-in. semiminor axis in the axial direction. The spherical dome cap has a 70.0-in. polar radius at XT = 951.526 in., a 211.855-in. spherical radius, and a 11.9-in. axial length. The aft Y-ring section of the tank indicated in figure 2 was modeled with four reference surfaces that connect the barrel to the aft dome and to the intertank. The reference surface that connects the barrel to the intertank is a 9.8-in-long, 165.373-in-radius cylinder. Two conical reference surfaces connect the barrel to the aft dome: the first is an 8.0-in-long cone with outer and inner polar radii equal to 165.373 in. and 164.72 in. at XT = 843 in. and XT = 851 in., respectively, and the second is a 4.273-in-long cone with outer and inner polar radii equal to 164.72 in. and 164.08 in. at XT = 851 in. and XT = 855.273 in., respectively. The fourth reference surface is a very short and essentially rigid cone that connects the aft end of the cylindrical surface to the intersection of the two conical sections. This cone was included in the model to represent adequately the stiffness of the Y-ring section where the shell segments join in order to prevent the Y-ring from passing through the adjacent shell walls during deformation. This modeling detail was also used to eliminate large artificial bending gradients in the Y-ring shell wall that caused convergence problems in the numerical solution of the nonlinear equations.

The SLWT LO_2 tank shell wall, chemically milled to reduce structural weight, has a highly variable thickness distribution. In the forward ogive, the thicknesses vary from 0.080 in. to 0.157 in. in both the meridional and circumferential directions. Similarly, in the aft ogive and barrel sections the thicknesses vary from 0.081 in. to 0.190 in. and from 0.140 in. to 0.385 in., respectively. In the aft dome the thicknesses vary from 0.088 in. to 0.125 in. This complex thickness distribution and corresponding wall eccentricities were input into the STAGS user-written subroutine WALL with FORTRAN statements. In addition, the LO_2 tank is thickened locally in several regions that support an external cable tray, and these local thicknesses were included in subroutine WALL.

Several meridional lines shown in figure 2 represent the weld lands of the gore and barrel panels that form the tank. These weld lands are substantially thicker than the adjacent shell wall, and their thicknesses vary in the meridional direction. The weld lands were modeled as discrete beams of rectangular cross section with variable width and depth. The variations in the weld-land cross-sectional geometry in the meridional direction were represented by using a linear variation with the corresponding surface arc length. The variable properties of the beams were input into STAGS with the user-written subroutine CROSS. The circumferential location of each weld land was specified to be at the column of nodes in the shell unit that is closest to its actual location. This approximation becomes more accurate when the

circumferential mesh density is increased. Circumferential weld lands are located where the forward and aft ogives are connected, where the T-ring attaches to the aft ogive and barrel, where the Y-ring attaches to the barrel and the aft dome, and where the elliptical part of the aft dome connects to the spherical cap. The weld lands located at the aft end of the barrel and elliptical dome were modeled as discrete rings for convenience, and all the other weld lands were modeled with shell elements. In addition, the two deep, thin-walled slosh baffle rings were modeled as discrete rings. The remainder of the slosh baffle was not included in the STAGS models because the stiffness and stability it provides to the slosh baffle rings are essentially included by modeling the slosh baffle rings as discrete rings.

Parts of the forward ogive fitting and the entire cover plate contain integrally machined stiffeners. These structures were modeled as an equivalent homogeneous orthotropic wall with the appropriate shell reference surface eccentricity. In addition, cutouts and other local details in the cover plate were neglected, and places in the ogive fitting and cover plate where the thickness is much larger than the nominal wall thickness were modeled using discrete rings.

Intertank Modeling Details

The reference surface for the intertank is a 270.35-in-long, 165.373-in-radius right-circular cylinder. The six skin-stringer panels of the intertank consist of external hat stiffeners bonded to a variable-thickness wall. The skin thicknesses (including primary doublers) range from 0.067 in. to 0.221 in. The hat stiffeners range in thickness from 0.045 in. to 0.063 in., are 2.50 in. deep, and taper in width from 2.57 in. at the shell wall to 1.38 in. at the top of the hat. The hat stiffener spacing is 7.20 in. The objective of the intertank model is to provide an accurate representation of the overall intertank stiffness so that load can be transferred to the LO_2 tank with as few finite-element degrees of freedom (DOF) as possible. To achieve this goal, the skin-stringer panels were modeled as an equivalent homogeneous orthotropic wall with a variable thickness that is eccentric to the shell reference surface. STAGS computed the equivalent homogeneous orthotropic wall properties by using the "smeared stiffener" capability of the user-written subroutines WALL and CROSS. This model includes the effects of all the hat stiffeners and the primary skin doubler plates. Eight extruded stringers fastened to four of the panels were not included in the model as discrete beams, but were approximated in a conservative manner as hat stiffeners with a maximum thickness of 0.63 in. The variable wall properties were input into STAGS with the user-written subroutine WALL. Cutouts in the panels, including the access door and its frame, were neglected based on the rationale that their influence on the transfer of load into the LO_2 tank is small.

The two thrust panels of the intertank are blade-stiffened panels integrally machined from a single piece of aluminum alloy. A total of 65 skin thicknesses that range from 0.090 in. in areas away from the central region of the panels to 2.062 in. in the area next to the SRB thrust fittings was used to model the thrust panels. A wall thickness of 2.062 in. was placed in the cutouts that house the SRB thrust fittings to facilitate load diffusion from the SRB beam to the thrust panels. The two internal longerons fastened to the thrust panels and the SRB beam, however, were neglected. Each panel has 26 variable-width blade stiffeners that are 2.06 in. deep. Thirty-six blade widths ranging from 0.180 in. to 1.050 in. were used to model the thrust panels as an equivalent homogeneous orthotropic wall with variable thickness in a manner similar to the skin-stringer panels.

The five internal ring frames and two (forward and aft) flanges of the intertank were modeled as discrete rings with variable and constant cross-sectional properties, respectively. For the ring frames, the section properties were modeled in a piecewise manner with constant properties for each beam element that connects two adjacent nodes. Because the discrete ring model of the ring frames does not account for lateral-torsional cross-sectional deformations, the effect of the roll ties shown in figure 3 is implicitly included. The SRB beam was also modeled as a discrete beam in which several beam elements were used to simulate its variable depth in a piecewise manner. The SRB beam, approximately 345 in. long, extends outboard of the shell reference surface to cause an eccentricity in the SRB interface forces of approximately 7 in., as shown in figure 4. Load diffusion from the ends of the SRB beam to the shell wall of the thrust panels is facilitated by connecting the node at each end of the SRB beam to the adjacent nodes on the thrust panels with high-stiffness beam elements.

Load Simulation

A primary goal of the SLWT LO_2 tank study presented herein was to determine how much additional load, beyond the operational loads, the tank can withstand before buckling or exhibiting severe bending gradients that will damage the thermal protection system (TPS). The basic approach used in the present study to achieve this goal is to apply all of the loads illustrated in figure 4 to the model, except for the SRB interface loads. The nodes on the ends of the SRB beam, where the SRB forces act, were restrained so that the SRB interface forces became reactions and rigid body motion was eliminated. Next, the applied loads were separated into two groups. The first group contained the LH_2 tank interface

force and moment, which were treated as the primary source of destabilizing compressive stresses in the LO_2 tank that may occur at load levels greater than the corresponding operational load level. The second group of loads consisted of the LO_2 pressure (for the second loading condition), the wind load, the structural weight, the thermal load, and the weight of the slosh baffle located inside the barrel section of the LO_2 tank. Constant in value, the loads in the second group were part of the operational loads considered to be passive loads when determining the stability margin of safety of the LO_2 tank.

The simple LO_2 pressure distribution and the temperature distribution were input into the STAGS model with the user-written FORTRAN subroutines UPRESS and UTEMP, respectively. The substantially more complicated wind load required construction of a Fourier series representation of the pressure field that was input directly into subroutine UPRESS. The slosh baffle weight of approximately 455 lb was applied to the slosh baffle support rings at $XT = 744.85$ in. and $XT = 851.0$ in. (fig. 2) as eccentric, uniformly distributed line loads. The LH_2 tank interface force and moment were applied to the model with the least squares loading and moving plane boundary features of STAGS. The STAGS least squares loading feature used a least squares fit to convert concentrated forces and moments applied at an axial location into statically equivalent shell-wall stress resultants. The moving plane boundary feature of STAGS enforced the geometric constraint that all nodes within the given plane remain coplanar during deformation.

In performing linear bifurcation buckling and nonlinear analyses with STAGS, two load factors, p_a and p_b, were assigned to the first (active) and second (passive) load groups, respectively. First, a linear analysis was conducted to verify that the SRB reactions calculated from the applied loads were reasonably close to the specified values defined previously. For both prelaunch loading conditions, the **i** and **k** components of the reactions were in good agreement with the corresponding specified values. In contrast, the **j** components of the reactions were not in very good agreement with the specified values. However, because the **j** components of the reactions act along the axis of the SRB beam, their effect is mostly contained within the intertank. As a result, the SRB beam reactions are reasonable approximations of the actual forces.

For the linear bifurcation buckling analyses, the load factor for the passive load group was assigned a value of one ($p_b = 1$), and the load factor for the active load group p_a was defined as the eigenvalue. This approach provided a linear prebuckling stress state in the model that was used in determining the eigenvalue. For the nonlinear analyses, the load factors for both load groups were increased simultaneously to a value of one ($p_a = p_b = 1$), which corresponds to the operational values of the loads and provides the proper nonlinear prebuckling state for the LO_2 tank. Then, the load factor p_a of the primary destabilizing loads was increased until an instability was reached.

SLWT Prelaunch Load Results

Results are presented in this section for the two prelaunch loading conditions previously discussed. First, results are presented for the loading condition that has a full LH_2 tank and an empty LO_2 tank. Then, results are presented for the loading condition that has a full LH_2 tank and a full LO_2 tank. For this second loading condition, results presented were obtained from STAGS models that neglect the slosh baffle ring stiffnesses. Other results obtained from models that include these ring stiffnesses show that neglecting the slosh baffle ring stiffnesses in the STAGS models yields similar structural deformations and conservative predictions of the LO_2 tank load-carrying capacity at load levels greater than the level of the operational loads.

Full LH_2 and Empty LO_2 Tanks

Several different finite-element meshes were used in the study for analysis of the LO_2 tank subjected to the prelaunch loading condition with a full LH_2 tank and an empty LO_2 tank. As a first step toward identifying an adequate mesh with as few degrees of freedom as possible, linear bifurcation buckling analyses were conducted. The passive loads associated with load factor p_b were applied to the STAGS models as a linear prebuckling stress state ($p_b = 1$), and the active (destabilizing) loads associated with load factor p_a were used to obtain the minimum eigenvalue.

The meshes investigated ranged from 104 600 to 213 500 DOF. The mesh identified as adequate for predicting the linear bifurcation buckling behavior is shown in figure 6 and corresponds to 146 700 DOF. This figure shows a buckle in the LO_2 barrel on the negative Y-axis side of the tank. The reduction in mesh size from 213 500 to 146 700 DOF was done by increasing the mesh fineness in the local region containing the buckle shown in figure 6 and then by eliminating unneeded mesh refinement elsewhere, with care not to introduce spurious solutions. This step was facilitated by the use of the five-node and seven-node rectangular transition elements available in STAGS. The 104 600- and 146 700-DOF models have the same general mesh arrangement shown in figure 6, but the level of local refinement of the mesh shown in figure 6 for the 146 700-DOF model is essentially twice that of the 104 600-DOF model. The eigenvalues for the

104 600- and 146 700-DOF models are given by $p_a = 3.36$ and $p_a = 3.26$, respectively. These values correspond to loads that are approximately three times the magnitude of the operational loads. Based on the smoothness of the buckling mode shown in figure 6 and the 3-percent difference in the eigenvalues, the 146 700-DOF model is considered adequate for representing the linear bifurcation behavior of the LO_2 tank for this loading condition.

Next, the 104 600- and 146 700-DOF models were used to conduct nonlinear analyses of a geometrically imperfect shell. An imperfection shape in the form of the corresponding linear bifurcation buckling mode and a negative value of the imperfection-amplitude-to-wall-thickness ratio $A/t = 0.25$ were used in these analyses. The thickness t in the ratio A/t, the minimum-gage wall thickness for the LO_2 barrel, has a value equal to 0.140 in. In general, the sign of the linear bifurcation buckling mode is arbitrary and is determined by the specific algorithm used to perform the calculations. For a shell structure with nonnegative Gaussian curvature, the sign of the eigenvector of the buckling mode indicates whether a specific region of the buckling mode of a curved surface is directed toward or away from the concave side of the surface. As a result, these two orientations of the same buckling mode generally correspond to different degrees of nonlinear interaction between imperfection shape and the membrane compressive stresses. In the study, the negative of the linear bifurcation buckling mode amplitude obtained from the STAGS models was used with the imperfection shape because it provided the strongest nonlinear interaction with the compressive stresses in the shell wall. The results of these analyses, shown in figure 7, are presented as a plot of load factor p_a versus the normal displacement of the shell wall at the largest crest of the buckle defined by the coordinates $XT = 787.97$ in. and $\theta = 300.94°$. (See fig. 2 for coordinate definitions.) The dashed and solid lines shown in the figure correspond to the 104 600-DOF and 146 700-DOF models, respectively. The unfilled square symbols and the filled circular symbols shown in the figure correspond to the actual analytical results obtained for the 104 600-DOF and 146 700-DOF models, respectively. The results shown in figure 7 indicate that there is a small discrepancy between the two nonlinear solutions. The solution for the more refined model has larger values of displacements for some values of the load factor. This discrepancy is attributed to the fact that the less refined model overestimates the bending stiffness of the shell wall. The results in figure 7 also suggest that the 146 700-DOF model is adequate for conducting nonlinear analyses for this loading condition.

Results obtained from nonlinear analyses for a geometrically perfect shell and for geometrically imperfect shells with values for the imperfection-amplitude-to-wall-thickness ratio $A/t = 0.25$, 0.5, and 1.0 appear in figure 8. These results were obtained with the 146 700-DOF model and with the imperfection shape in the form of the corresponding linear bifurcation buckling mode with a negative amplitude. The filled circles in the figure indicate solutions for the geometrically perfect shell, and the unfilled squares, triangles, and circles indicate solutions for the geometrically imperfect shells with $A/t = 0.25$, 0.5, and 1.0, respectively. The horizontal dashed line represents the linear bifurcation buckling load level. The results shown in figure 8 are presented as a plot of the load factor p_a versus the normal displacement of the shell wall at the largest crest of the buckle, defined by the coordinates $XT = 789.939$ in. and $\theta = 301.64°$. These results indicate that the barrel section of the LO_2 tank, where the buckles appear, exhibits stable postbuckling load-carrying capacity for the geometrically imperfect shells and, as a result, is insensitive to initial imperfections. Moreover, the shallowness of the barrel panel that contains the buckle and the presence of stable postbuckling load-carrying capacity suggest that the buckling behavior is essentially that of the stable-symmetric bifurcation type; that is, the unstable-asymmetric bifurcation behavior usually associated with singly curved panels is essentially benign.

The buckle patterns obtained from the linear bifurcation analysis and the nonlinear analyses are all very similar in shape and occur in the same location. The stress distribution in the shell that causes the buckle pattern to form is shown in figure 9 for a geometrically perfect shell and for $p_a = p_b = 1$. Contours of the membrane meridional and shear stresses on the negative Y-axis side ($\theta = 270°$) of the tank are shown in figures 9(a) and 9(b), respectively, in units of psi. These contours indicate that high meridional compression stresses exist above the thrust panel as expected. The contours also indicate that buckling occurs in a region of the barrel where there are significant shear stresses in the shell that interact with the meridional compressive stresses and reduce the buckling load.

Full LH_2 and LO_2 Tanks

Several different finite-element meshes were used for the analysis of the LO_2 tank subjected to the prelaunch loading condition with full LH_2 and LO_2 tanks. Linear bifurcation buckling analyses were conducted first to identify an adequate mesh for modeling the behavior of the shell with as few degrees of freedom as possible. The passive loads associated with load factor p_b were applied to the STAGS models as a linear prebuckling stress state ($p_b = 1$), and the active (destabilizing) loads associated with load factor p_a were used to obtain the minimum eigenvalue.

The meshes investigated for this prelaunch loading condition ranged from 48 990 to 121 500 DOF. The mesh identified as adequate for predicting linear bifurcation buckling, which appears in figure 10, corresponds to 99 100 DOF. The reduction in mesh size from 121 500 to 99 100 DOF was achieved by increasing the mesh in the region surrounding the buckle and then eliminating unneeded mesh refinement elsewhere in a manner similar to that used for the previous loading condition. A 79 950-DOF model was investigated that has the same general mesh arrangement as that shown in figure 10, but the local refinement shown on the right side of the ogive was used for both locally refined regions of the ogive. The eigenvalues for the 79 950- and 99 100-DOF models are given by $p_a = 3.94$ and $p_a = 3.78$, respectively, where a value of 1.0 corresponds to the magnitude of the operational loads. Because of the smoothness of the buckling mode shown in figure 10 and the 4-percent difference in the eigenvalues, the 99 100-DOF model was used to represent the linear bifurcation behavior of the LO_2 tank for this loading condition. The 79 950- and 99 100-DOF models also were used to obtain nonlinear solutions for a geometrically perfect shell. These solutions, which are in excellent agreement, indicate that the 99 100-DOF model adequately represents the nonlinear behavior of the LO_2 tank for this loading condition. Thus, all subsequent results presented in this section were obtained with the 99 100-DOF model.

A short-wavelength buckle in the forward part of the aft ogive, shown in figure 10, is essentially a wrinkle in the skin on the negative *Y*-axis side of the tank. The loads acting along the shell meridians near the SRB attachment point develop the meridional compressive stress resultants shown in figure 11(a) (given in lb/in. for $p_a = p_b = 1$) that caused the buckling mode shown in figure 10. Insight into the formation of the buckling mode is obtained by noting that Gaussian curvature is a geometric measure related to how much the shell membrane stiffness participates in its bending deformations. The results in figure 11 indicate that the meridional compressive stress resultants and the circumferential tension stress resultants increase in the LO_2 tank from the tip of the forward ogive to the intertank. The magnitude of the shell Gaussian curvature decreases in this part of the shell, which causes local buckling to occur at this location. In the forward ogive, there are relatively small values of hoop tensile stresses to stabilize the shell, but the Gaussian curvature is high. In the aft ogive, the meridional compressive stresses and hoop tensile stresses are larger than in the forward ogive, but the Gaussian curvature is much smaller. The STAGS results suggest that the higher values of meridional compressive stresses and lower values of Gaussian curvature in the aft ogive are the dominant factors that influence the location of the buckling mode. These findings also indicate that the shortness of the half-wavelength of the buckling mode is a result of the high values of the circumferential tensile stress resultants shown in figure 11 that are caused by the hydrostatic pressure exerted on the shell wall by the LO_2.

Results obtained from nonlinear analyses of a geometrically perfect shell and a geometrically imperfect shell with an imperfection-amplitude-to-wall-thickness ratio $A/t = 0.3$ are presented in figures 12 and 13, respectively. The thickness t in the ratio A/t is the minimum-gage wall thickness of the aft ogive and has a value equal to 0.100 in. The results shown in figure 13 were obtained using an imperfection shape in the form of the corresponding linear bifurcation buckling mode with a negative amplitude. The negative of the linear bifurcation buckling mode amplitude obtained was used as the imperfection shape because it provided the strongest nonlinear interaction with the compressive stresses in the shell wall. The results shown in these two figures are for nonlinear solutions that were obtained by increasing the load factors p_a and p_b simultaneously to a value of one and then holding p_b constant while increasing the magnitude of the load factor p_a. The normal displacements along the length of the aft ogive shell wall are represented by the solid lines in the figures for values of the load factor p_a approximately equal to 3.0, 4.0, and 5.0. The linear bifurcation mode is represented by the dashed line in the figures, with normalized amplitudes given by the right-hand ordinate of the figures. The bifurcation mode in the figures indicates how the imperfection shape influences the nonlinear solution. The solid lines shown in the figures predict a short-wavelength bending response in the aft ogive over the negative *Y*-axis ($\theta = 270°$) that is similar in shape to the corresponding linear bifurcation buckling mode shape. The overall slope of the solid lines (obtained by fitting a straight line to each curve) in the figures results from the outward displacement of the shell wall caused by the increase in pressure as p_a and p_b are simultaneously increased to a value of one in the nonlinear analysis. This effect is not represented in the linear prebuckling stress state used in a linear bifurcation buckling analysis and, as a result, does not affect the overall slope of the dashed lines.

The results presented in figures 12 and 13 predict a stable nonlinear response at load levels greater than the load predicted by the linear bifurcation buckling analysis ($p_a = 3.78$). As the load increases, substantial bending gradients (indicated by the waviness of the curves) develop and grow in the shell wall, which reduces the apparent meridional stiffness of the aft ogive. The nonuniformity of the bending gradients is caused by the thickness variations in the ogive and the presence of the weld lands. These results indicate that a geometrical imperfection in the shape of the linear bifurcation

buckling mode and with a small negative amplitude will greatly increase the severity of the bending gradients and will cause the growth of the bending gradients to start at much lower load levels.

The reduction in apparent meridional stiffness of the aft ogive is shown more explicitly in figure 14. In this figure, the intensities of the bending gradients (indicated by the magnitude of the normal displacement amplitude) at XT = 637.66 in. for the geometrically perfect shell (x = 99.3 in. in fig. 12) and at XT = 633.77 for the geometrically imperfect shell (x = 95.4 in. in fig. 13) are given as a function of the load factor p_a. These locations represent the locations of the largest bending gradients shown in figures 12 and 13. The amplitude Δw shown in figure 14 is the distance from the maximum value of the local shell-wall displacement to the adjacent minimum value and represents the intensity of the local bending gradient in the response. The filled circles shown in the figure correspond to results for a geometrically perfect shell, and the unfilled triangles and squares correspond to results for geometrically imperfect shells with imperfection-amplitude-to-wall-thickness ratios of A/t = 0.1 and 0.3, respectively (t = 0.100 in.). The horizontal dashed line shown in the figure represents the linear bifurcation buckling load level.

The results shown in figure 14 indicate that the amplitude of the greatest local bending gradient grows with increasing load and that the amount of growth increases substantially with increasing geometric imperfection amplitude. The results predict that the shell can support loads greater than the critical buckling load predicted by a linear bifurcation buckling analysis. As Δw increases, the apparent meridional stiffness decreases, and as a result, the positive-valued constant of proportionality between an increment in load and the corresponding increment in displacement amplitude decreases. This trend is manifested by the reduction in slope of the load versus displacement amplitude curves. This type of response is similar to the response reported by Stevens, Starnes, and Almroth in reference 2 for cylindrical shells subjected to combined internal pressure and a pure bending moment. The results in reference 2 indicate that the amplitude of the short-wavelength deflection approaches a horizontal tangent as the load increases and that the value of the load for the horizontal tangent corresponds to a local collapse mode of the cylinder. Mathematically, the horizontal tangent indicates that unbounded growth of the displacement occurs for an infinitesimal increase in the load. It is expected that the curves shown in figure 14 would approach a horizontal tangent as Δw increases until a redistribution in load occurs within the aft ogive. As a horizontal tangent in a load versus displacement amplitude curve is approached, the region of the shell containing the bending gradients becomes incapable of supporting additional load, and the compressive load is redistributed to another portion of the aft ogive. If other parts of the ogive cannot support the compressive load, the shell will collapse. However, if other parts of the ogive can support the compressive load, the slope of the load-versus-displacement amplitude curve will increase as the loading increases. Geometric imperfections with large amplitudes also could cause a similar redistribution in load, and as a result, the corresponding slope of the load-versus-displacement amplitude curve would increase. Similar curves for smaller geometric imperfection amplitudes would approach a horizontal tangent.

The results presented in figures 12 through 14 indicate that large local bending gradients may occur in the shell wall for loads that are much smaller than the local collapse load and may cause the TPS to debond from the shell wall and fail. The results presented in figure 15 indicate approximate estimates of the local radius of curvature for the largest bending gradient in the aft ogive along the negative Y-axis ($\theta = 270°$). These bending gradients are located at XT = 637.66 in. for the geometrically perfect shell (x = 99.3 in. in fig. 12) and at XT = 633.77 in. for the geometrically imperfect shells (x = 95.4 in. in fig. 13). The local radius of curvature ρ shown in the right-hand sketch of the figure was calculated by the formula

$$\rho = \frac{[1 + (w')^2]^{3/2}}{|w''|}$$

where w, the local displacement shown in the right-hand sketch in figure 15, is approximated by $w = (\Delta w/2)\sin(2\pi x/\lambda)$ where λ is the buckle wavelength. The prime marks in the equation denote differentiation with respect to the local x coordinate. At the crests of the wave defined by $x = \lambda/4$ and $3\lambda/4$, $w' = 0$, and the radius of curvature is given by $\rho = \lambda^2/(2\pi^2\Delta w)$. The filled circles shown in the figure correspond to results for the geometrically perfect shell, and the unfilled triangles and squares correspond to results for geometrically imperfect shells with imperfection-amplitude-to-wall-thickness ratios of A/t = 0.1 and 0.3, respectively. The imperfection shape is identical to the linear bifurcation buckling mode with a negative amplitude shown in figure 13. The results in figure 15 demonstrate that the geometric imperfection amplitude has a significant influence on the local radius of curvature of the shell wall. For example, if a given thermal protection system is known to debond from the shell wall at a value of ρ = 100 in., the maximum load factor is reduced from a value of approximately 4.8 for the geometrically perfect shell to 3.2 for the geometrically imperfect shell with A/t = 0.3.

SWT Full-Scale Structural Test Results

To assess the accuracy of the STAGS model of the SLWT LO_2 tank, finite-element anaylses were performed on two full-scale structural tests using the same modeling approach described previously. The two full-scale tests were conducted at the NASA George C. Marshall Spaceflight Center on the original SWT during the development program of the original Space Shuttle ET. Precise measurements of initial geometric imperfections in the tank wall were not made for either of these test specimens. As a result, these test results can be used only as a qualitative means for assessing the accuracy of the STAGS model of the SLWT LO_2 tank.

The SWT LO_2 tank has essentially the same geometry as the SLWT LO_2 tank, but is made of 2219 aluminum alloy. The primary difference between the two LO_2 tanks is that the skins of the SWT are thicker than those of the SLWT, with the thicknesses much more uniformly distributed over the SWT shell. Thus, the modeling approach described for the SLWT was used to model the two full-scale SWT test articles. The SWT model was generated by modifying the STAGS user-written subroutine WALL for the SLWT to account for the SWT thicknesses. The differences between the SWT intertank and the SLWT intertank are negligible for the purpose of transferring loads from the intertank to the LO_2 tank. The two full-scale SWT tests described subsequently are referred to herein as the structural test article (STA) and the ground vibration test article (GVTA).

STA Results

The STA consisted of a SWT LO_2 tank and a SWT intertank mounted vertically to a LH_2 tank load simulator and two rigid vertical posts at the SRB attachment points. The LH_2 tank load simulator was modeled by a self-equilibrated line load applied to the bottom of the intertank, as indicated in figure 16. A uniformly distributed circumferential line load of 1394 kips was also applied to the tank at XT = 852.8 in. For the test, these two loads were applied and then the tank was filled with room temperature water while an ullage pressure was maintained in the tank. After filling the tank to XT = 455 in., a depth of approximately 42 ft, the ullage pressure was slowly reduced. When the ullage pressure reached 0.57 psig, the tank unexpectedly buckled in the forward ogive between XT = 455 in. and XT = 475 in. and between θ = 253° and 277° (negative Y-axis side of the tank). The SRB interface forces that are reacted at the two vertical posts had magnitudes equal to 1295 kips (fig. 16).

To simulate the test loading conditions in a practical manner, all loads shown in figure 16, except for the SRB beam loads, were controlled by the load factor p_a. A value of p_a = 1 corresponds to values of the loads at which the actual test article buckled. The loads at the ends of the SRB beam were computed as reactions and found to be in excellent agreement with the corresponding SRB beam loads shown in figure 16.

Finite-element meshes were constructed for the STA and a limited convergence study was performed that followed an approach similar to that described for the SLWT analyses. The final mesh used to analyze the STA has 159 993 DOF and is highly refined in the forward ogive on the negative Y-axis side of the tank. The linear bifurcation buckling mode obtained for the STA with this mesh is shown in figure 17. This buckling mode is a short-wavelength buckle similar to the one obtained for the SLWT prelaunch loading condition with full LH_2 and LO_2 tanks. The location of the buckling mode shown in this figure is the same as the location observed during the test. The eigenvalue is given by p_a = 1.14.

Next, a series of nonlinear analyses were conducted using the 159 993-DOF mesh for values of the imperfection-amplitude-to-wall-thickness ratio A/t = 0, 0.1, 0.25, 0.5, and 1.0. The thickness t in the ratio A/t is the minimum-gage wall thickness of the forward ogive and has a value equal to 0.080 in. For each of these cases, the geometric imperfection shape was input in the form of the linear bifurcation buckling mode shown in figure 17, with a negative amplitude to obtain the strongest interaction between the membrane compressive stress and shell-wall deformations.

Figure 18 shows the results of the nonlinear analyses of the STA. The maximum normal displacement that occurs at the crest of the buckle pattern is shown in the figure as a function of the load factor p_a. The buckle crest is located at XT = 457.6 in. and XT = 466.6 in. for the geometrically perfect and imperfect shells, respectively, and at θ = 267.2°. The filled circles and the unfilled circles, diamonds, squares, and triangles correspond to results for A/t = 0, 0.1, 0.25, 0.5, and 1.0, respectively. The results for all values of A/t indicate a monotonic increase in load with increasing normal displacement. However, a maximum load was reached at which numerical difficulties were encountered in the nonlinear solutions. After several unsuccessful tries to increase the load above these values, it was concluded that the last data point on each curve corresponds to a limit point of the shell response. At each limit point, the shell buckled into a mode similar in shape to the buckling mode shown in figure 17 and at the same location. The meridional and circumferential stress resultant distributions are similar to those presented in figure 11 for the prelaunch loading condition with full LH_2 and LO_2 tanks.

The values of the limit points (filled circles) are shown in figure 19 as a function of geometric imperfection amplitude and load factor, and indicate the

imperfection sensitivity of the STA. The limit points obtained for the STA span a broad load range bounded by p_a = 1.18 for a geometrically perfect shell and p_a = 0.53 for a geometrically imperfect shell with A/t = 1.0 (A = 0.080 in.). This load range corresponds to a 55-percent reduction in load-carrying capacity of a geometrically perfect shell. The dashed line shown in the figure has a value of A/t = 0.064 for p_a = 1 (which corresponds to the buckling load of the test). This result suggests that the STAGS modeling approach provides a reasonably accurate indication of the SWT behavior. Because of the similar geometric character of the SWT and the SLWT, the results also suggest that the SLWT model should provide a reasonable representation of the SLWT nonlinear shell response.

GVTA Results

The GVTA consisted of a SWT mounted on two SRBs and an orbiter attached to the SWT. The SWT consisted of a LO_2 tank, a LH_2 tank, and an intertank. In this configuration, the SWT is inclined at an angle of approximately 10° in the *XT-Z* plane because of the eccentric weight of the orbiter. The loads acting on the LO_2 tank and intertank during the test and the inclination angle α are shown in figure 20. These loads consist of two SRB interface force components, the LH_2 tank interface force and moment, a uniformly distributed circumferential line load of 20.86 kips applied at XT = 852.8 in., and a hydrostatic water pressure distribution that corresponds to the tank fill level of XT = 645 in. (a depth of approximately 26.5 ft). No ullage pressure was present inside the LO_2 tank during the test. The hydrostatic pressure distribution for the GVTA was defined in the STAGS model with user-written subroutine UPRESS in terms of the local axial coordinate x shown in figure 20(b). The pressure distribution is given by $p(x, \theta) = 0$ for values of $x \le x_f - r(x) \tan\alpha \cos\theta$, where x_f is the local coordinate of the fill level defined by the positive numerical difference between stations XT = 645 in. and XT = 371 in., as shown in figure 20(b). The symbol θ is the cylindrical coordinate defined in figure 2, and $r(x)$ is the polar radius of the shell reference surface (fig. 20(b)) that was calculated from the differential geometry of the LO_2 tank components. For the remaining values of x, the pressure is given by

$$p(x, \theta) = \gamma[(x - x_f) \cos\alpha + r(x) \sin\alpha \cos\theta]$$

where γ represents the specific weight of water at room temperature.

The original test plan for the GVTA was to fill the tank with water and then to perform a ground vibration test. However, when the water level reached XT = 645 in., the tank unexpectedly buckled in the forward ogive between approximately XT = 437 in. and XT = 503 in. and between θ = 247° and 281° (negative Y-axis side of the tank).

The test loading conditions for the GVTA were simulated in the manner described herein for the STA; that is, all loads shown in figure 20, except for the SRB interface forces, were assigned to the load factor p_a such that a value of p_a = 1 corresponds to buckling of the test article. The loads at the ends of the SRB beam were computed as reactions and found to be in excellent agreement with the SRB interface forces shown in figure 20(a).

Several finite-element meshes were also investigated for the GVTA following the same approach used for the STA. The final mesh selected to analyze the GVTA has 252 300 DOF and is highly refined in the forward ogive on the negative Y-axis side of the tank. The linear bifurcation buckling mode obtained for the GVTA with this mesh is shown in figure 21. This buckling mode is also a short-wavelength buckling mode similar to the one obtained for the SLWT prelaunch loading condition with full LH_2 and LO_2 tanks and for the STA. The location of the buckling mode shown in this figure is essentially the same as the location observed during the test. The eigenvalue is given by p_a = 2.41.

Next, the 252 300-DOF mesh was used to conduct nonlinear analyses for values of the imperfection-amplitude-to-wall-thickness ratio A/t = 0, 0.125, 0.25, 0.5, 0.75, and 1.0. The minimum-gage wall thickness t for the forward ogive has a value equal to 0.080 in. For each of these cases, the geometric imperfection shape was in the form of the linear bifurcation buckling mode shown in figure 21 with a negative amplitude.

The results of the nonlinear analyses of the GVTA are shown in figure 22. The maximum normal displacement that occurs at the crest of the buckle pattern is located at XT = 466.7 in. and at θ = 267.2°, and is shown in the figure as a function of the load factor p_a. The filled squares, triangles, and circles and the unfilled circles, squares, and triangles correspond to results for A/t = 0, 0.125, 0.25, 0.5, 0.75, and 1.0, respectively. Similar to the STA results, the GVTA results indicate a monotonic increase in load with increasing normal displacement that terminates at a limit point for all values of A/t. At each limit point, the shell buckles into a mode similar in shape to the mode shown in figure 21, and at the same location. The values of the limit points (filled circles) shown in figure 23 as a function of the geometric imperfection amplitude and load factor indicate the imperfection sensitivity of the GVTA. The limit points obtained for the GVTA span a broad load range bounded by p_a = 2.46 for a geometrically perfect shell and p_a = 0.92 for a geometrically imperfect shell with A/t = 1. This load range corresponds to a 62-percent reduction in the load-carrying

capacity of a geometrically perfect shell. The load reduction for the GVTA is approximately 7 percent greater than that for the STA. The dashed line shown in figure 23 has a value of $A/t = 0.625$ ($A = 0.050$ in.) for $p_a = 1$ (which corresponds to the buckling load of the test). This result also suggests that the STAGS modeling approach provides a reasonably accurate indication of the SWT behavior and the SLWT nonlinear shell response.

Concluding Remarks

The results of buckling and nonlinear analyses of the Space Shuttle superlightweight tank (SLWT) liquid-oxygen (LO_2) tank have been presented. An overview of the LO_2 tank and intertank structures and the loading conditions for two important prelaunch loading conditions have been described. In addition, the analysis code used in the study has been described and the finite-element modeling approach and details presented. The analytical method used in the study to simulate the loading conditions associated with prelaunch fueling of the Space Shuttle has been discussed.

Results have been presented for the superlightweight LO_2 tank subjected to two prelaunch loading conditions and for two full-scale structural tests that were conducted during the development program of the original standard-weight tank (SWT). These results illustrate three distinctly different types of nonlinear response for thin-walled shells subjected to combined mechanical and thermal loads that may be encountered in the design of other liquid-fuel launch vehicles. Predicting the response of these shells generally requires large-scale, high-fidelity finite-element models to represent the response accurately. For the first SLWT prelaunch loading condition, the liquid-hydrogen (LH_2) tank is full and the LO_2 tank is empty. The analytical results predict that the nonlinear response is characterized by a buckling response that is insensitive to initial geometric imperfections. For this loading condition, the barrel section of the LO_2 tank is predicted to buckle at loads that are more than twice the operational loads. For the second SLWT prelaunch loading condition, the LH_2 and LO_2 tanks are full. The nonlinear response for this loading condition is characterized by a short-wavelength bending gradient that grows in amplitude in a stable manner with increasing load. For this loading condition, local bending gradients appear in the aft ogive of the LO_2 tank that do not lead to a general instability mode but may cause failure of the thermal protection system for load levels in excess of approximately twice the operational load level. Moreover, the results predict that the severity of the local gradients is significantly affected by localized initial geometric imperfections.

For the two full-scale structural tests of the SWT, the nonlinear responses exhibit local buckling of a doubly curved shell segment of the LO_2 tank forward ogive that is characterized by a limit-point behavior. The magnitude of the load level corresponding to the limit point has been shown to be very sensitive to local initial geometric imperfections in the LO_2 tank. Specifically, load reductions of about 55 to 62 percent of the buckling load of a geometrically perfect shell are predicted for a geometric imperfection shape in the form of the linear bifurcation buckling mode and with a one-wall-thickness imperfection amplitude. The buckling loads obtained from both tests correspond to geometric imperfection amplitudes that are less than one minimum-gage wall thickness. For both tests, the analytical results suggest that the finite-element modeling approach used in the present study represents the nonlinear behavior of the superlightweight LO_2 tank very well.

NASA Langley Research Center
Hampton, VA 23681-0001
September 18, 1996

References

1. Brogan, Frank A.; Rankin, Charles C.; and Cabiness, Harold D.: *STAGS User Manual*. LMSC P032594, June 1994.

2. Stephens, Wendell B.; Starnes, James H., Jr.; and Almroth, B. O.: Collapse of Long Cylindrical Shells Under Combined Bending and Pressure Loads. *AIAA J.*, vol. 13, no. 1, Jan. 1975, pp. 20–25.

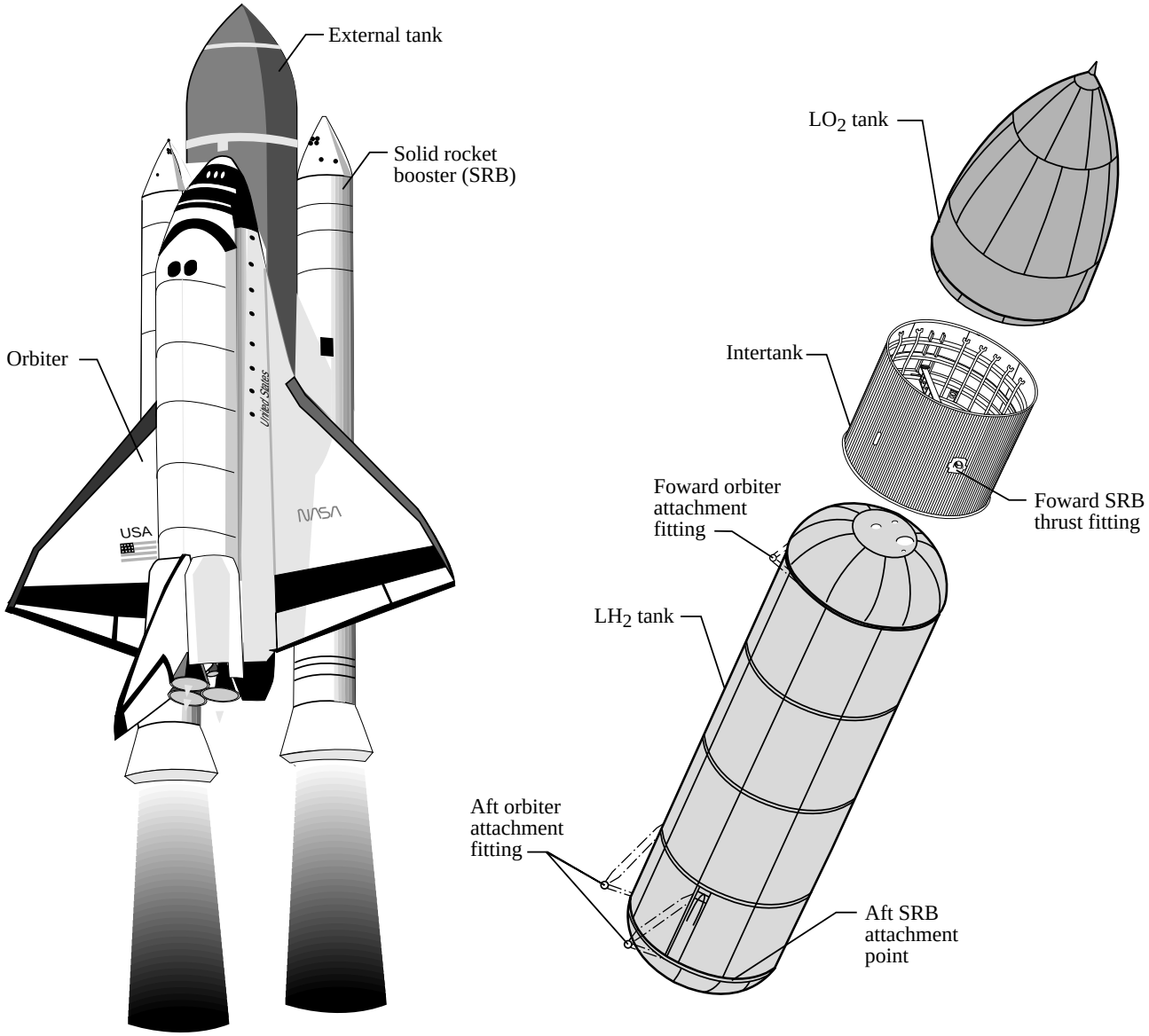

Figure 1. Space Shuttle external tank components.

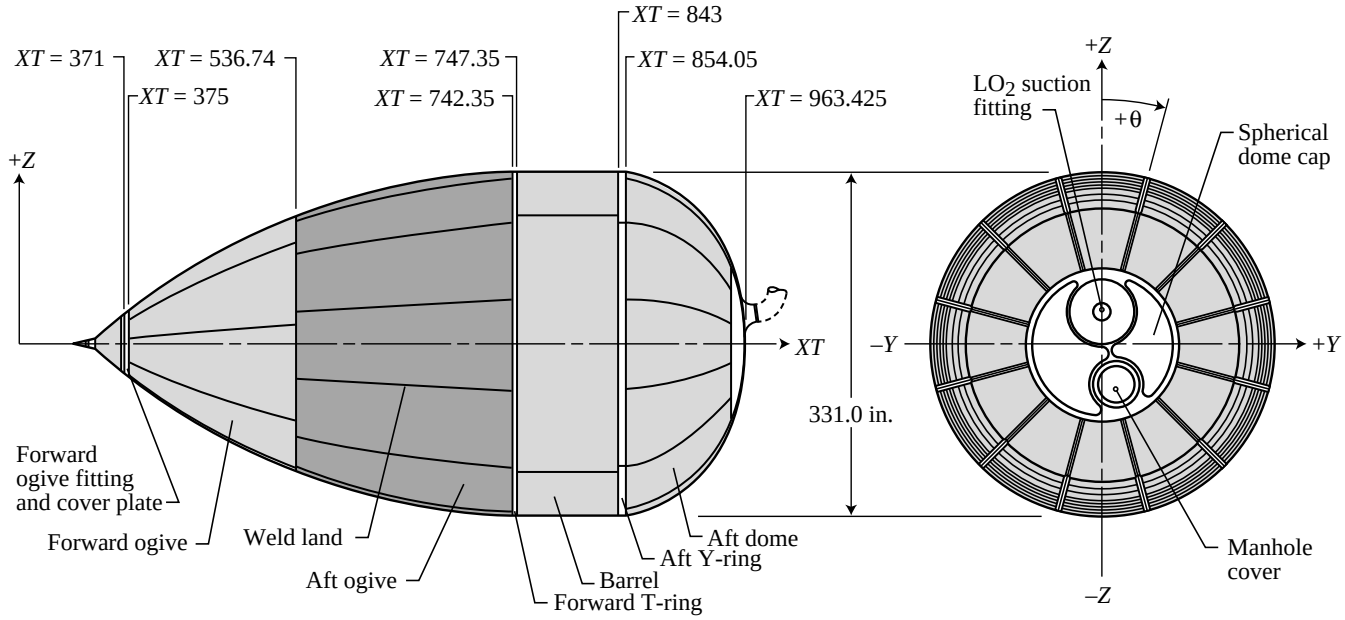

Figure 2. LO_2 tank structural components. *XT* values in inches.

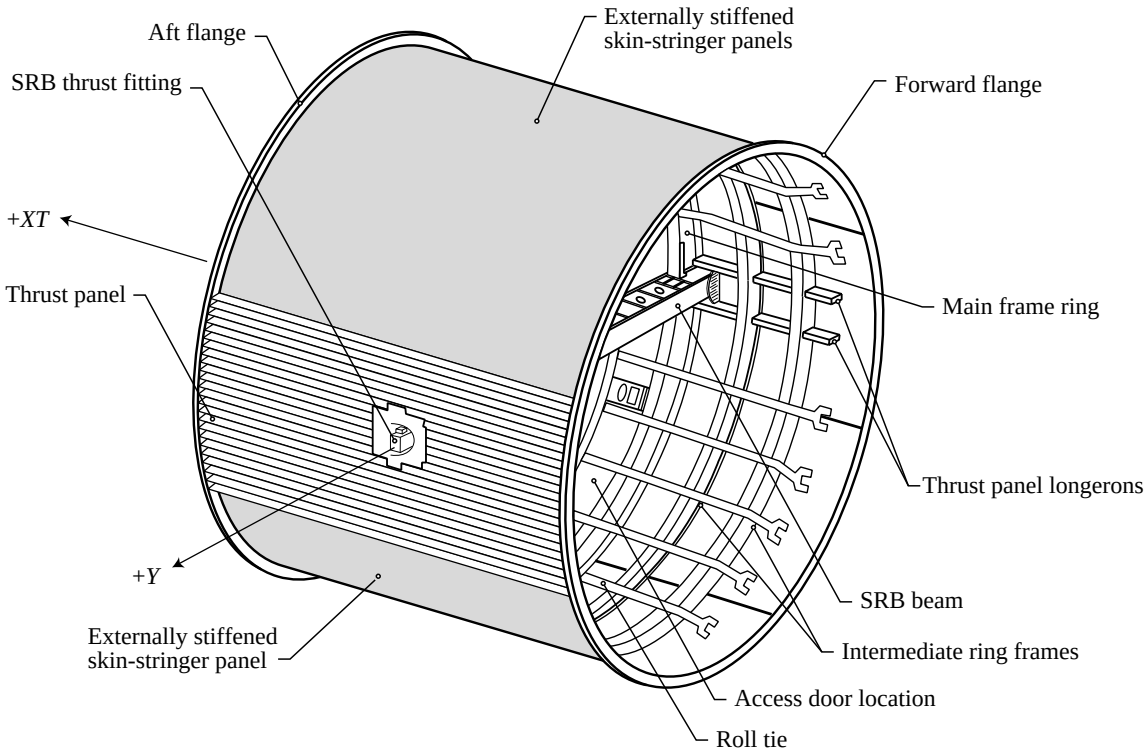

Figure 3. Intertank structure.

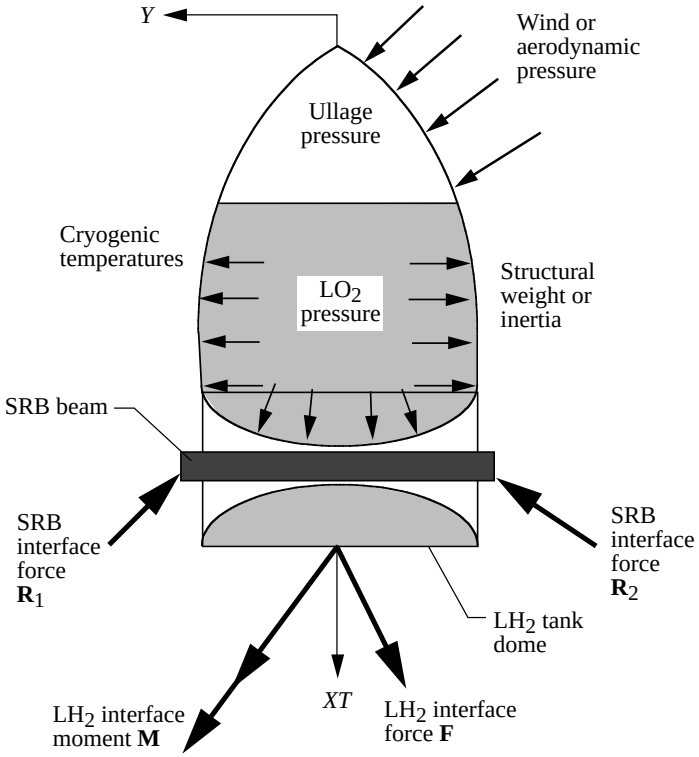

Figure 4. Loading characteristics.

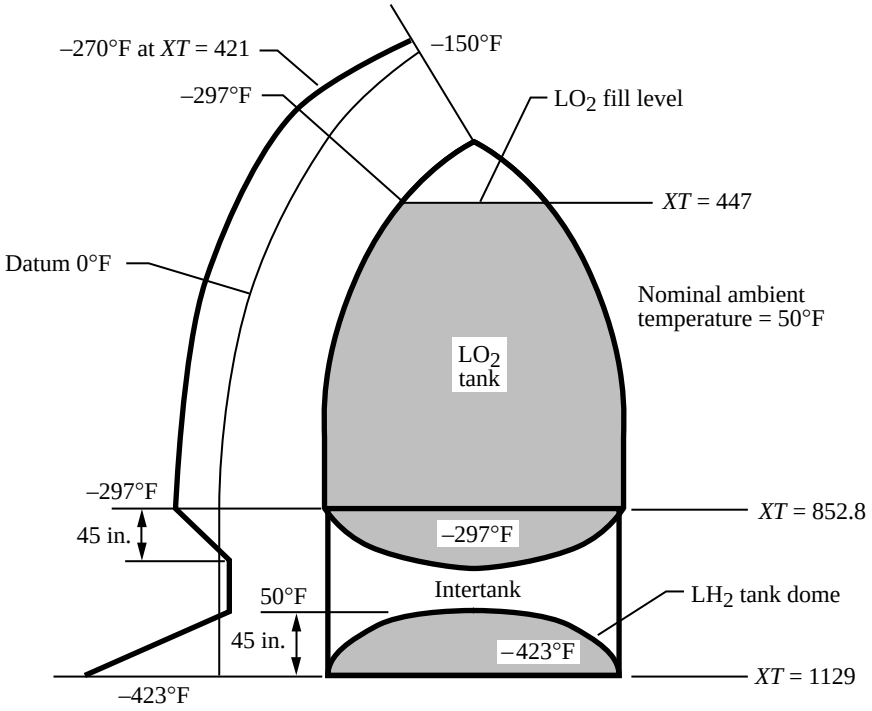

Figure 5. Axisymmetric temperature profile for prelaunch loading condition with full LH_2 and LO_2 tanks. *XT* values in inches.

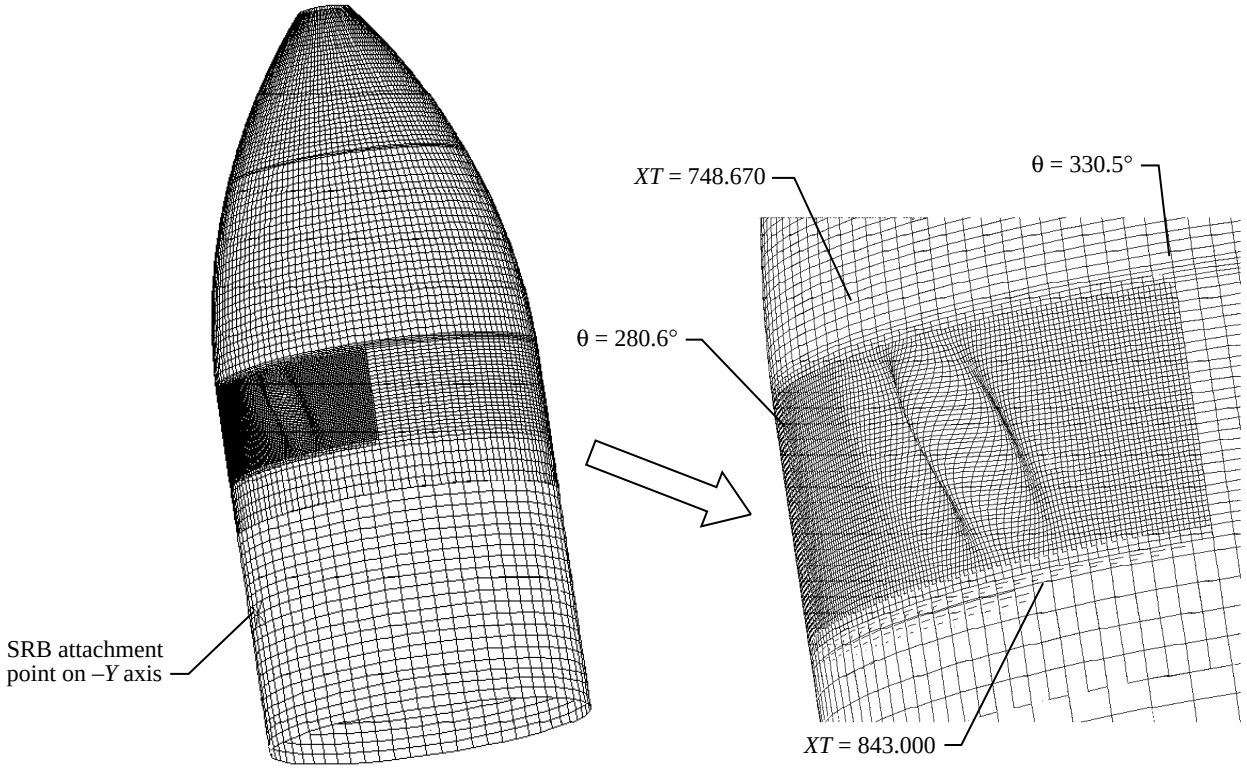

Figure 6. Linear bifurcation buckling mode for prelaunch loading condition with full LH_2 tank and empty LO_2 tank. 146 700 DOF; *XT* values in inches.

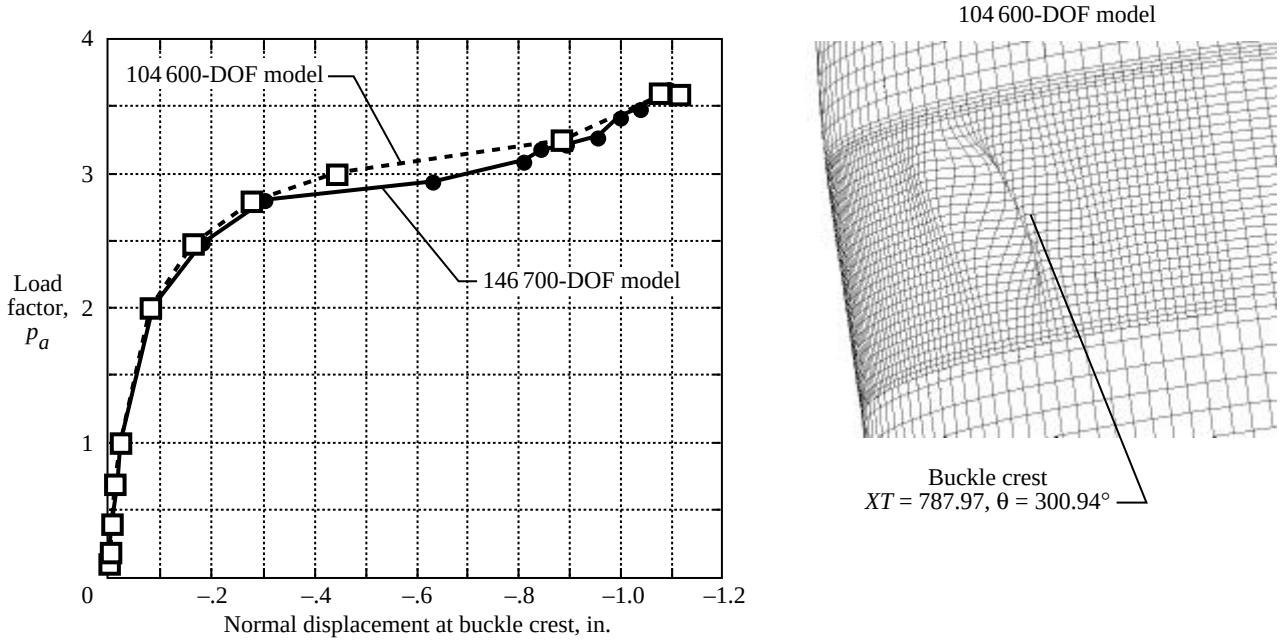

Figure 7. Convergence of nonlinear solutions for prelaunch loading condition with full LH_2 and empty LO_2 tanks. Imperfection-amplitude-to-wall-thickness ratio $A/t = 0.25$; *XT* value in inches.

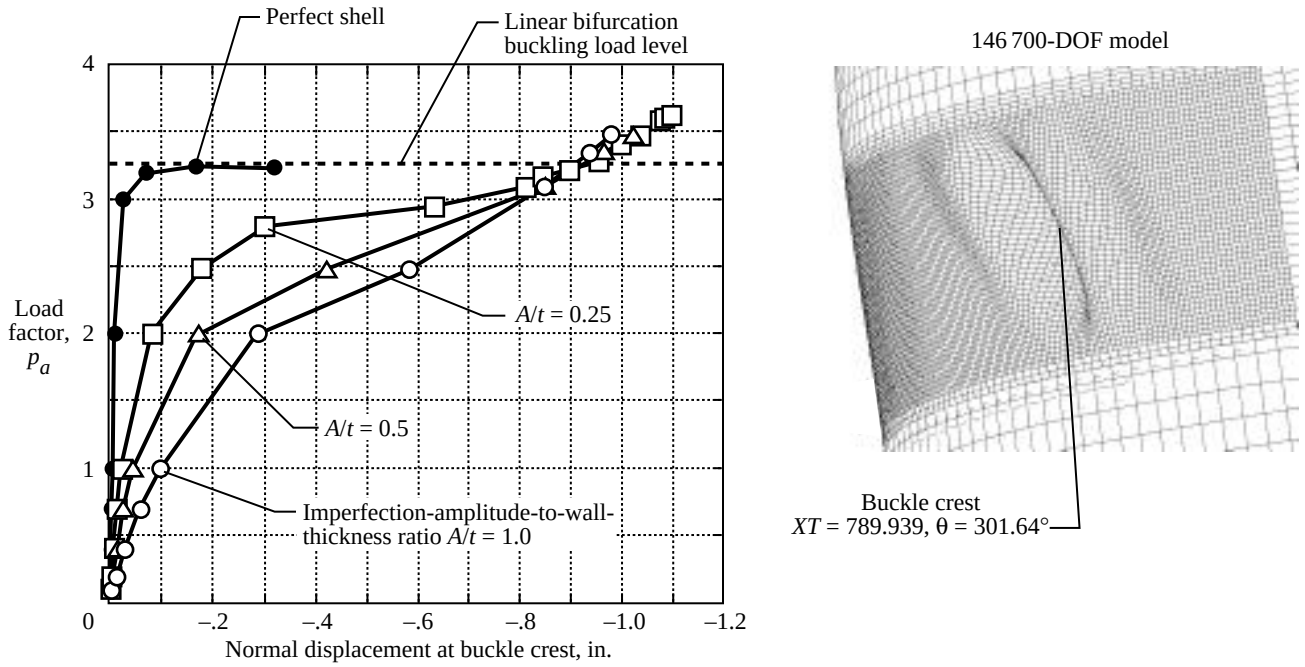

Figure 8. Effect of imperfection amplitude on nonlinear solutions for prelaunch loading condition with full LH_2 and empty LO_2 tanks. *XT* value in inches.

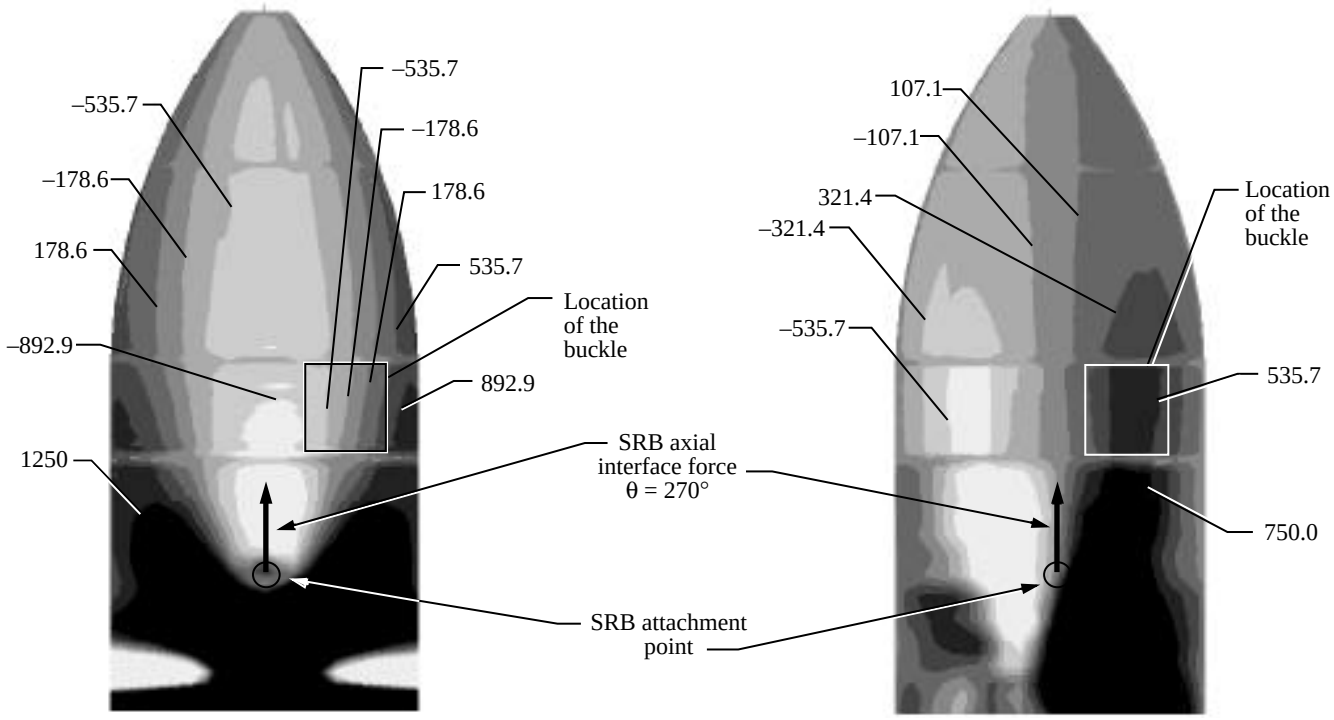

(a) Meridional stress.

(a) Shear stress.

Figure 9. Membrane stress distributions in geometrically perfect LO_2 tank and intertank for prelaunch loading condition with full LH_2 and empty LO_2 tanks. $p_a = p_b = 1$; stress values in psi.

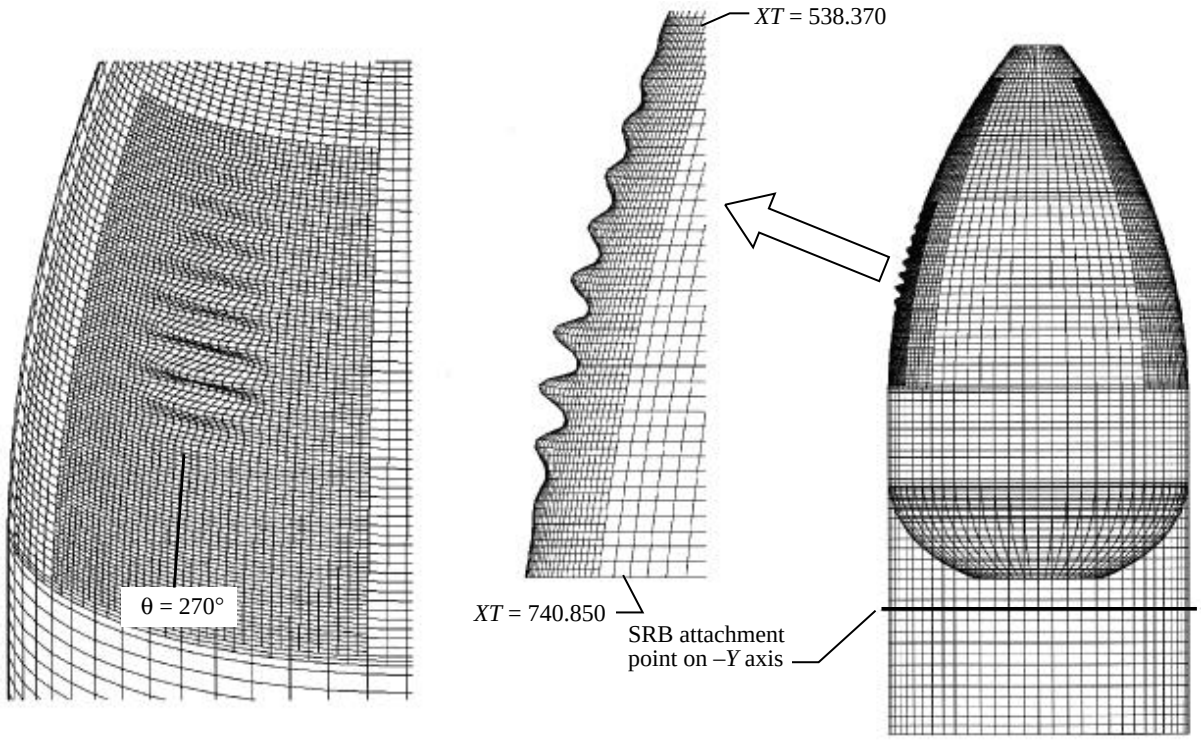

(a) Rotated view. (b) Side view.

Figure 10. Linear bifurcation buckling mode for prelaunch loading condition with full LH_2 and LO_2 tanks. 99 100 DOF; *XT* values in inches.

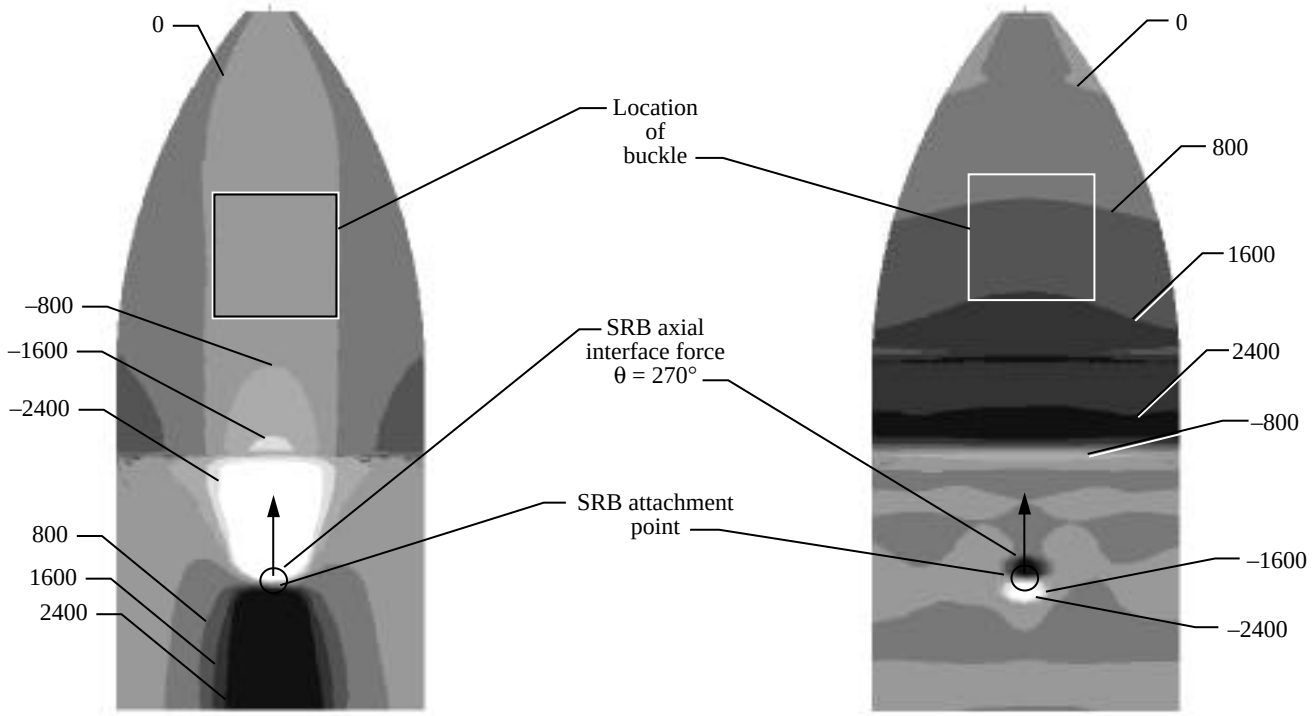

(a) Meridional stress resultant.

(b) Circumferential stress resultant.

Figure 11. Stress distributions in geometrically perfect LO_2 tank and intertank for prelaunch loading condition with full LH_2 and LO_2 tanks. $p_a = p_b = 1$; stress resultant values in lb/in.

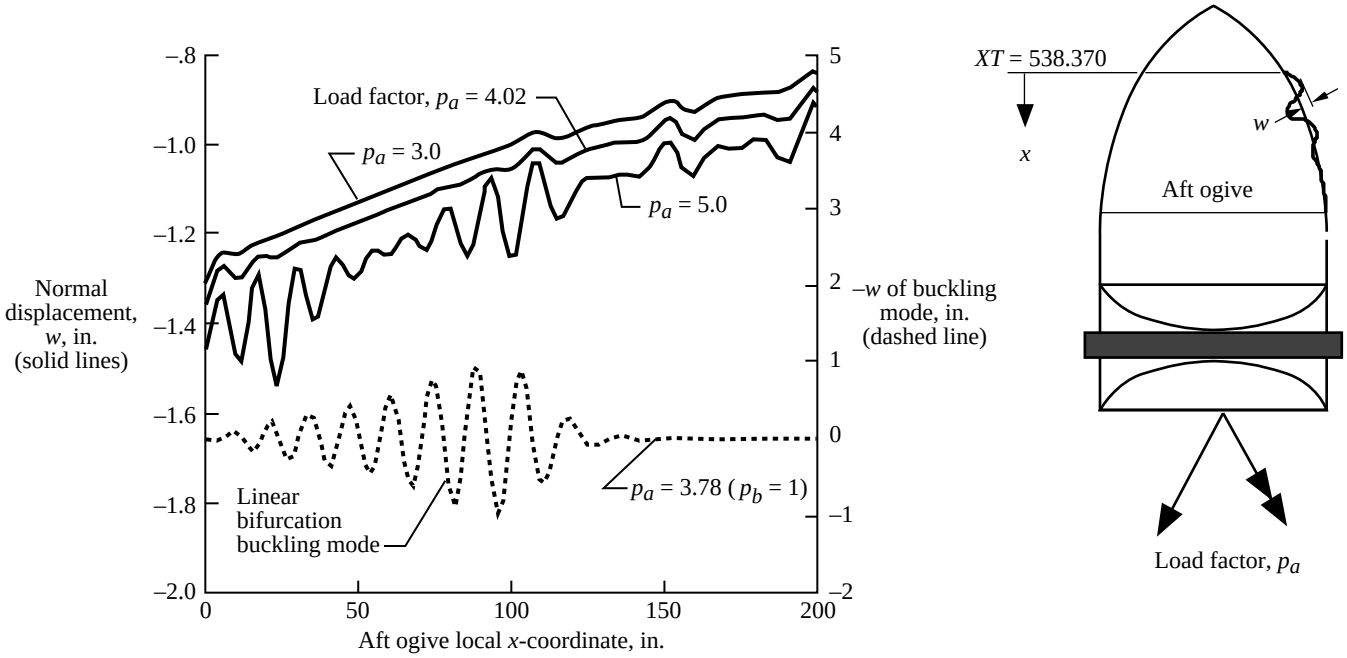

Figure 12. Bending gradients in aft ogive of geometrically perfect LO_2 tank shell for prelaunch loading condition with full LH_2 and LO_2 tanks for θ = 270°. *XT* value in inches.

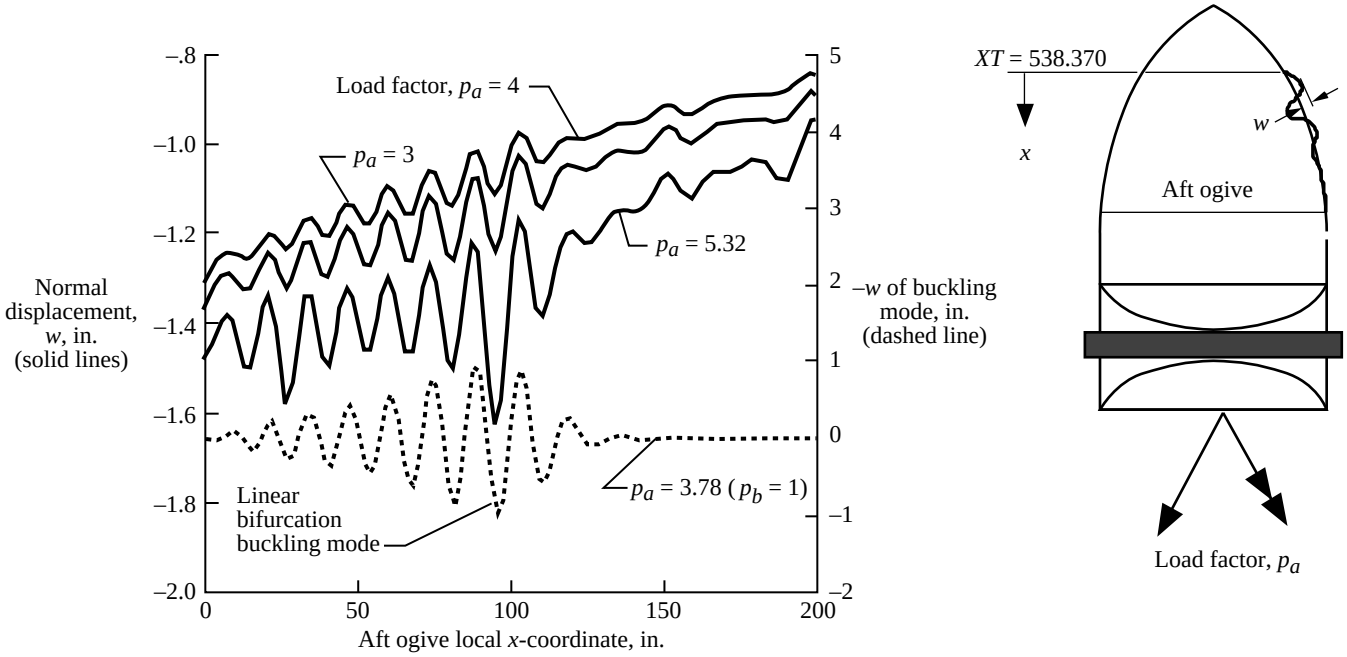

Figure 13. Bending gradients in aft ogive of geometrically imperfect LO_2 tank shell for prelaunch loading condition with full LH_2 and LO_2 tanks for θ = 270°. Imperfection-amplitude-to-wall-thickness ratio A/t = 0.3; *XT* value in inches.

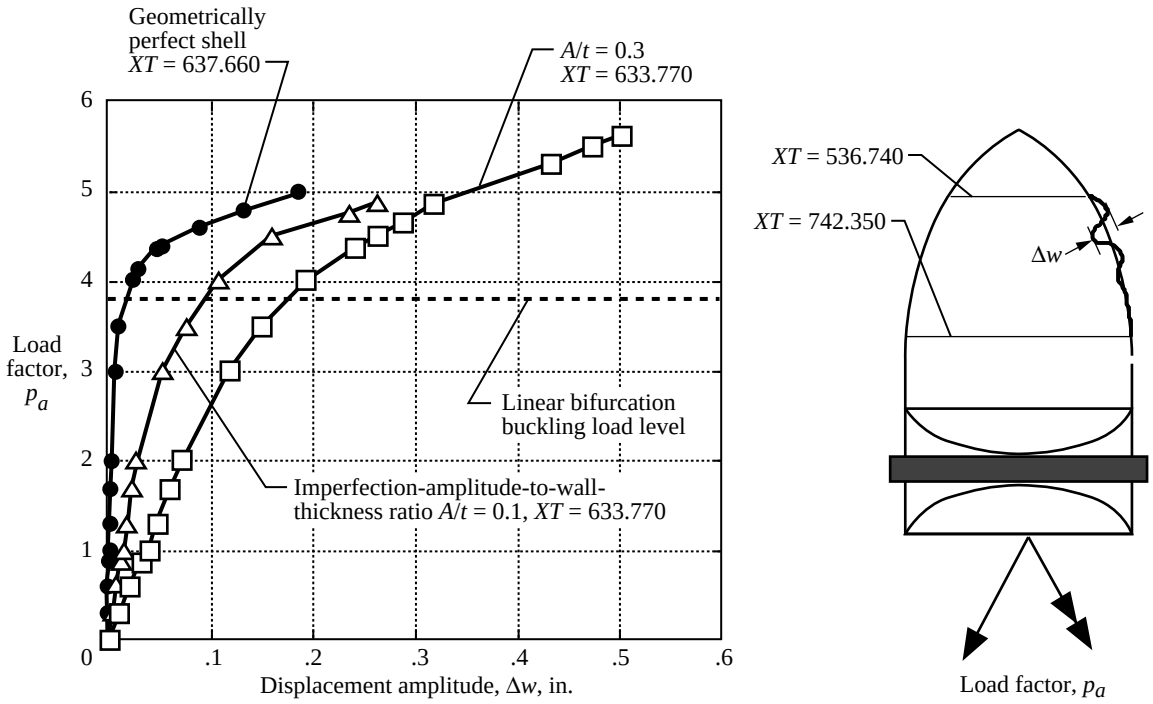

Figure 14. Effect of imperfection amplitude on nonlinear solutions for prelaunch loading condition with full LH_2 and LO_2 tanks for θ = 270°. *XT* values in inches.

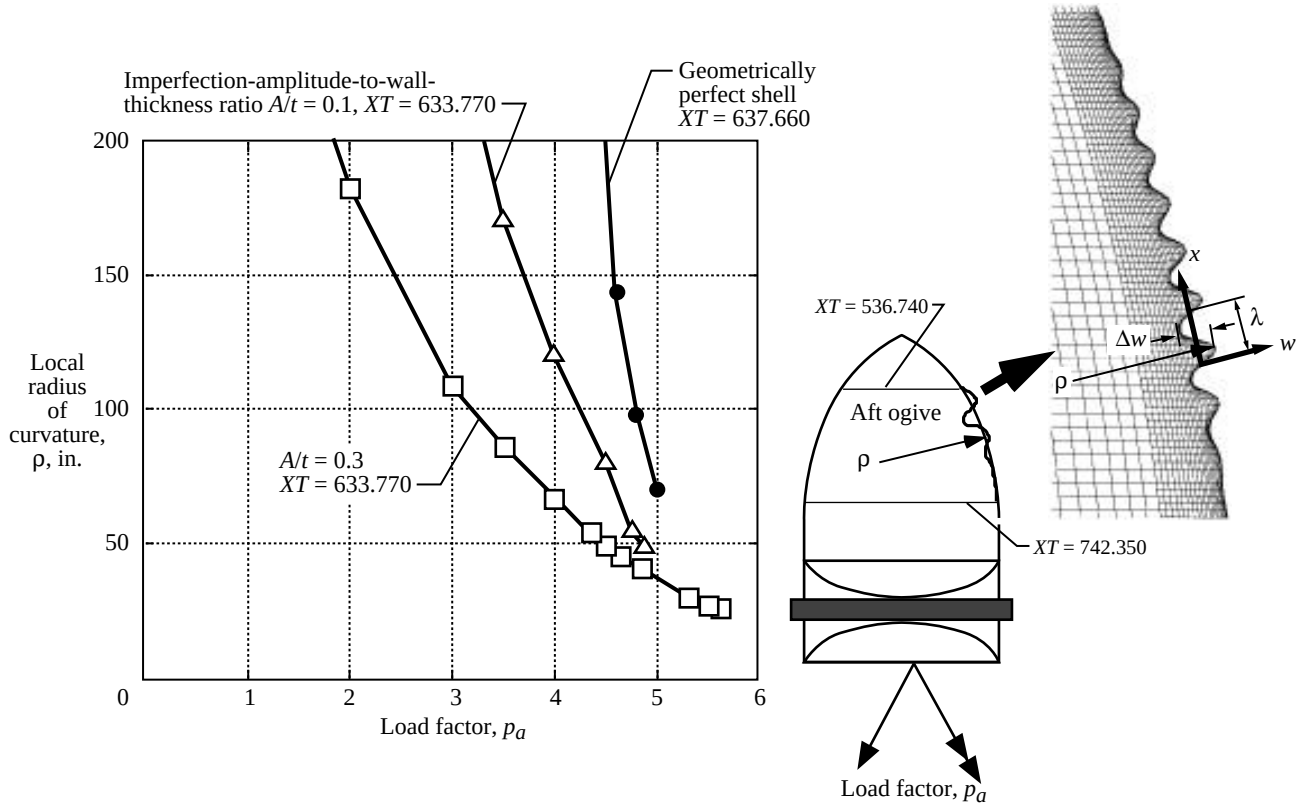

Figure 15. Effect of imperfection amplitude on local radius of curvature of largest bending gradient for prelaunch loading condition with full LH_2 and LO_2 tanks for θ = 270°. *XT* values in inches.

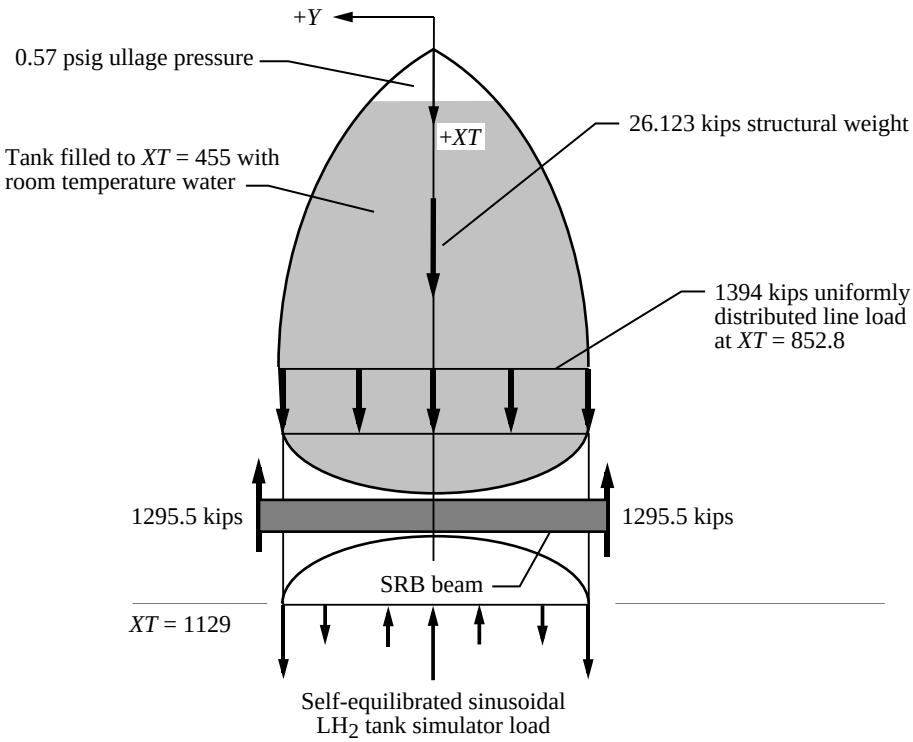

Figure 16. Loads for SWT STA at buckling. *XT* values in inches.

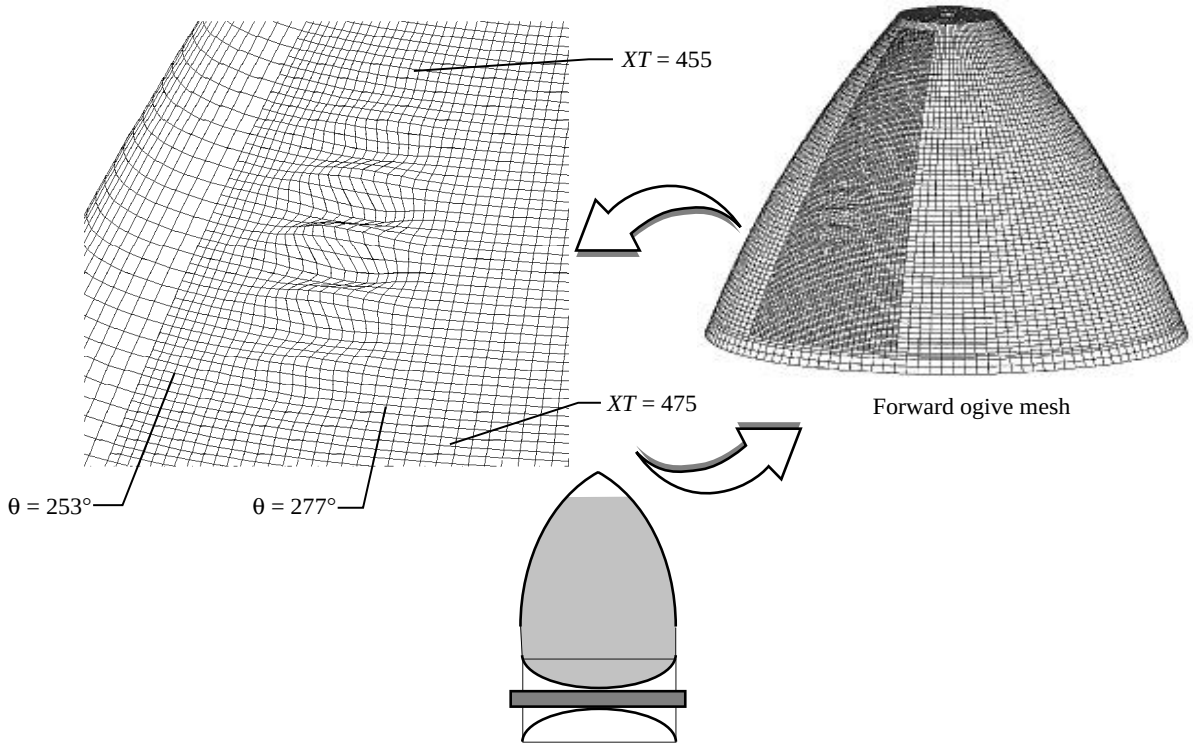

Figure 17. Linear bifurcation buckling mode for STA, 159 993 DOF. *XT* values in inches.

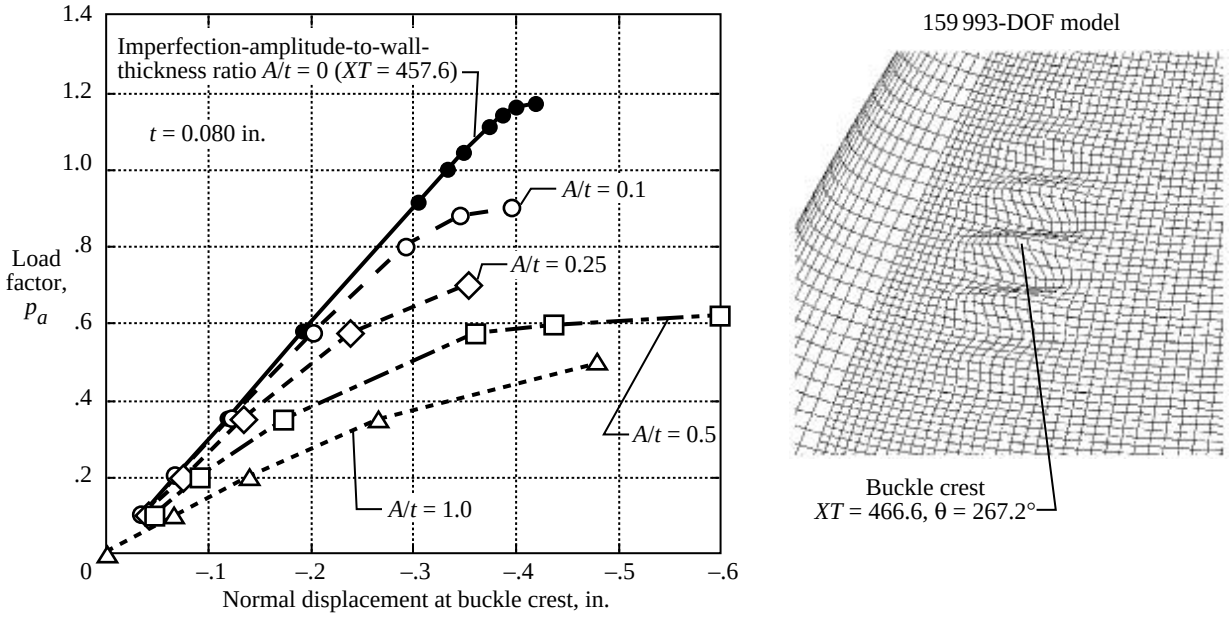

Figure 18. Effect of imperfection amplitude on collapse load for STA. *XT* values in inches.

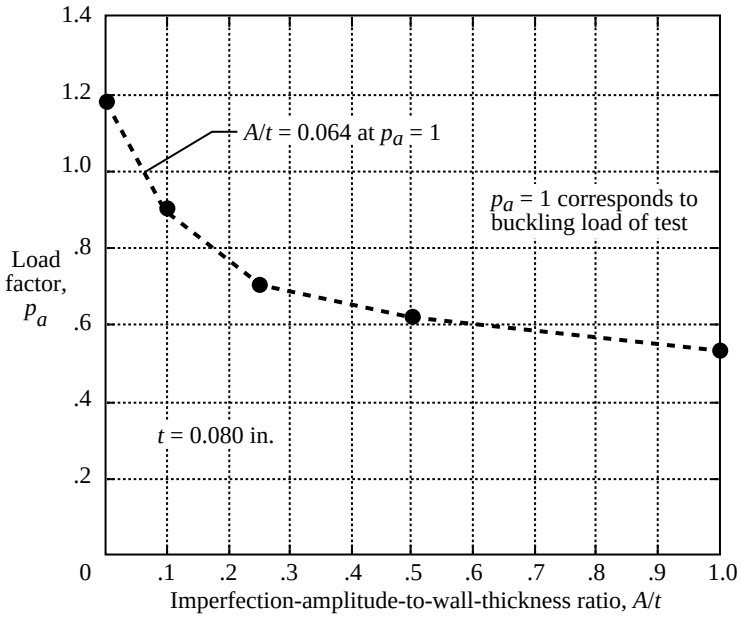

Figure 19. Predicted imperfection sensitivity of STA.

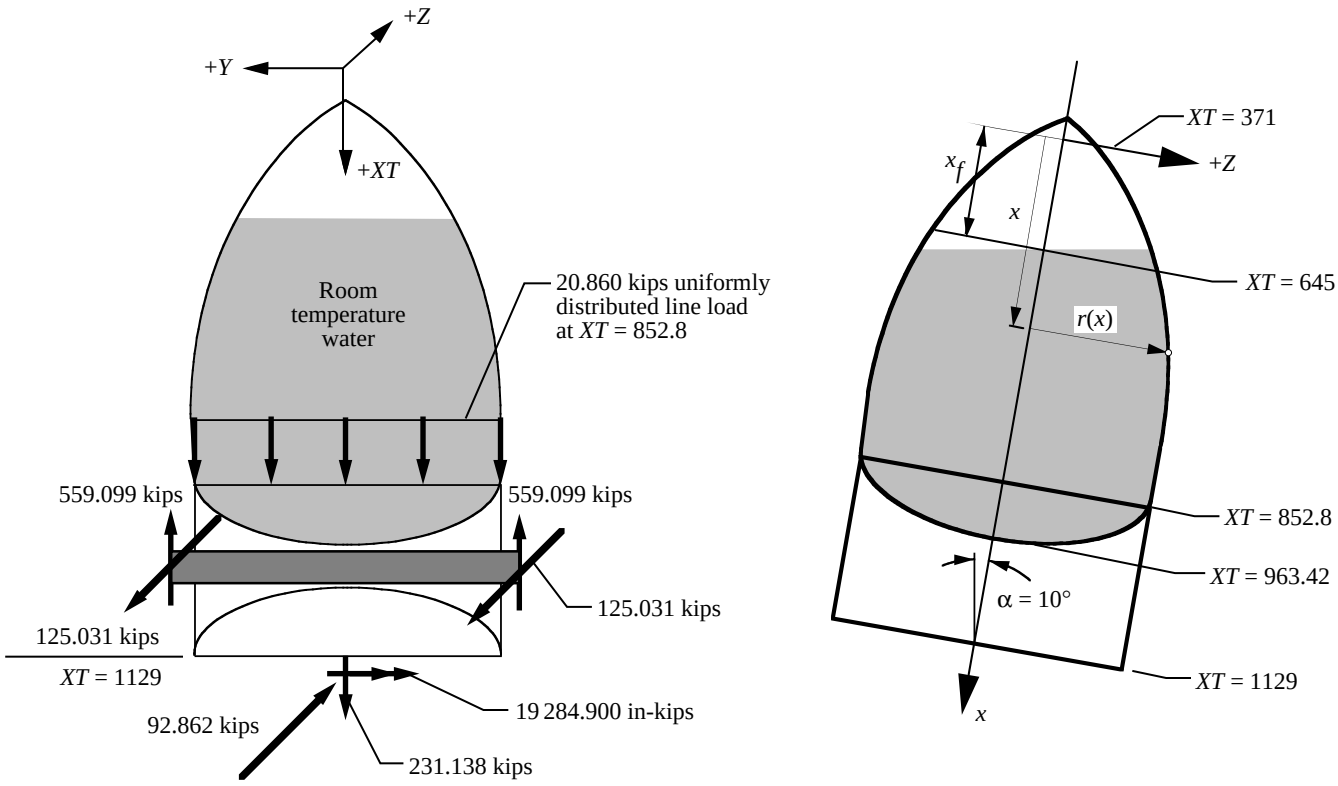

(a) Front view. (b) Side view.

Figure 20. Loads for SWT GVTA at buckling. XT values in inches.

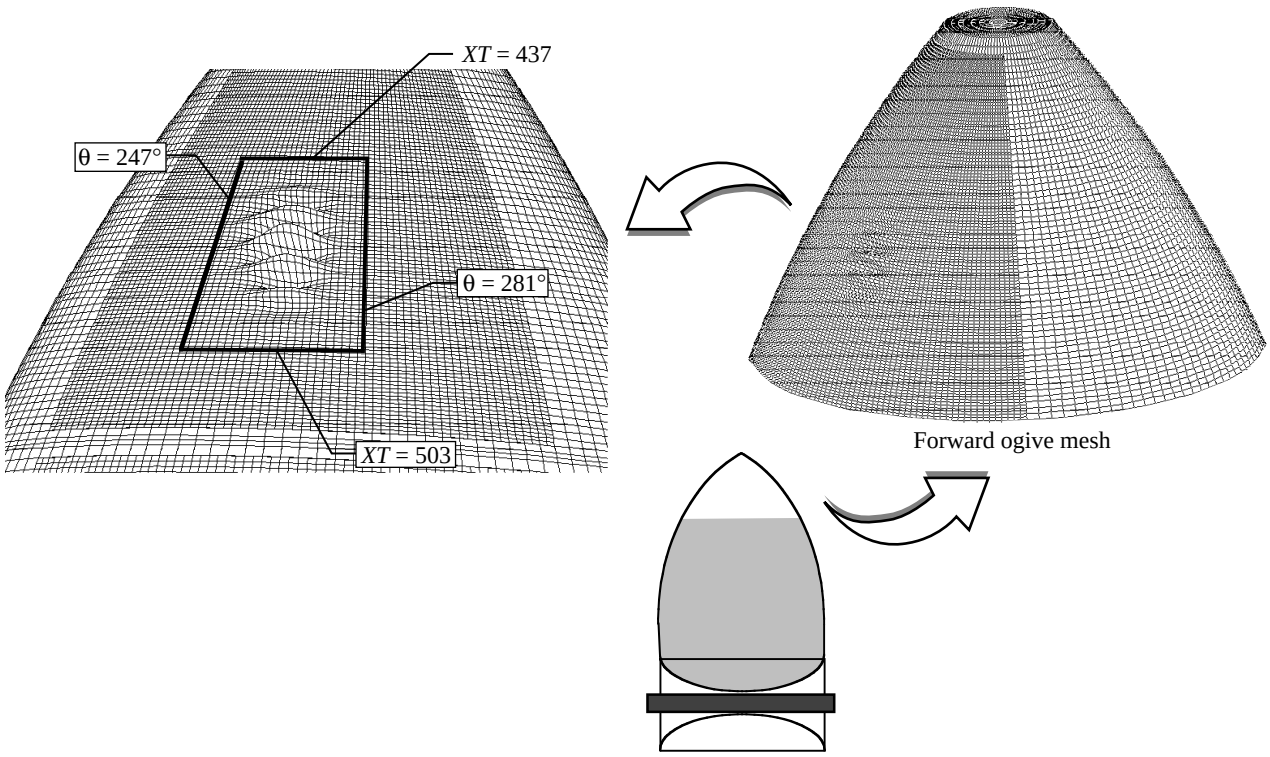

Figure 21. Linear bifurcation buckling mode for GVTA. 252 300 DOF; *XT* values in inches.

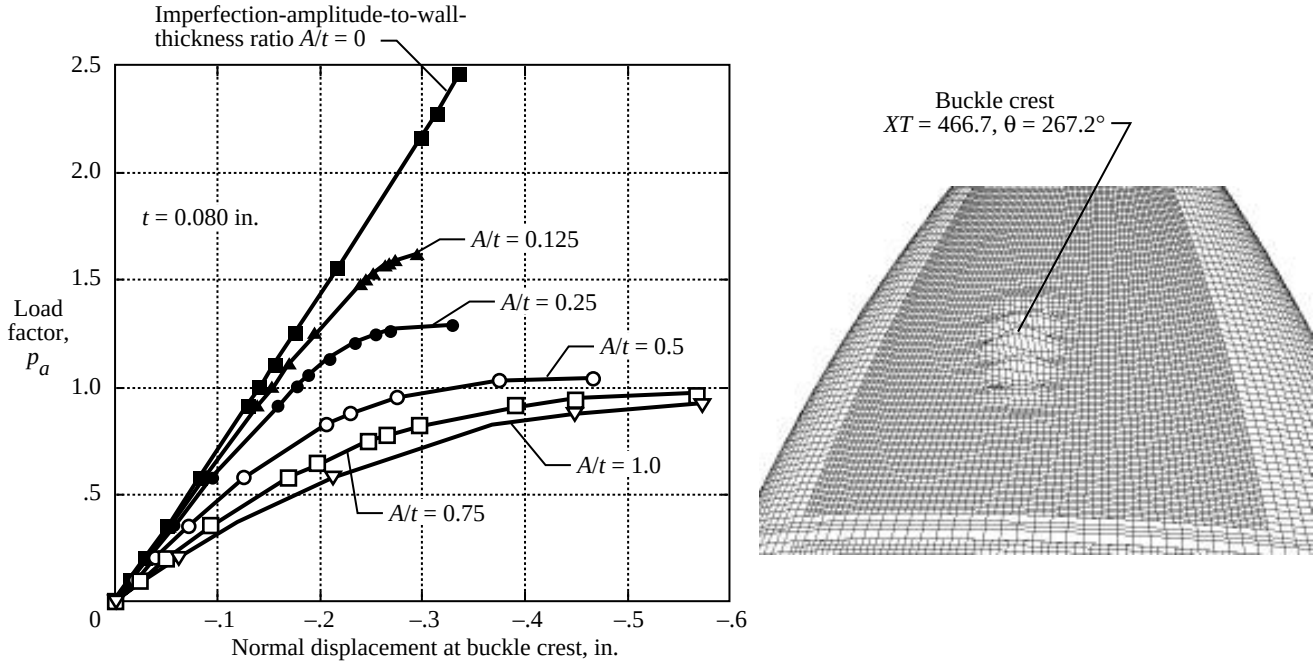

Figure 22. Effect of imperfection amplitude on buckling load for GVTA. *XT* values in inches.

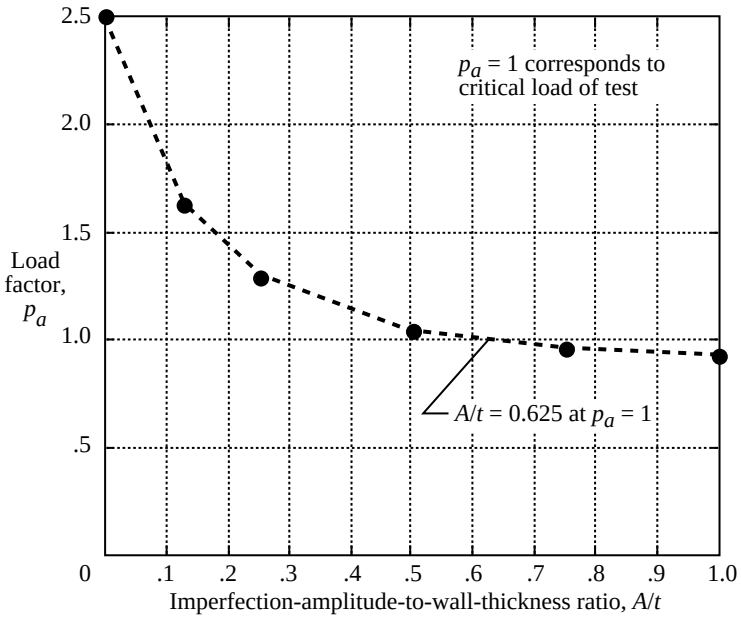

Figure 23. Predicted imperfection sensitivity of GVTA.

REPORT DOCUMENTATION PAGE

Form Approved
OMB No. 0704-0188

1. AGENCY USE ONLY *(Leave blank)*	2. REPORT DATE	3. REPORT TYPE AND DATES COVERED
	December 1996	Technical Paper

4. TITLE AND SUBTITLE
Nonlinear Analysis of the Space Shuttle Superlightweight External Fuel Tank

5. FUNDING NUMBERS
WU 505-63-50-08

6. AUTHOR(S)
Michael P. Nemeth, Vicki O. Britt, Timothy J. Collins, and James H. Starnes, Jr.

7. PERFORMING ORGANIZATION NAME(S) AND ADDRESS(ES)
NASA Langley Research Center
Hampton, VA 23681-0001

8. PERFORMING ORGANIZATION REPORT NUMBER
L-17564

9. SPONSORING/MONITORING AGENCY NAME(S) AND ADDRESS(ES)
National Aeronautics and Space Administration
Washington, DC 20546-0001

10. SPONSORING/MONITORING AGENCY REPORT NUMBER
NASA TP-3616

11. SUPPLEMENTARY NOTES
Presented at the 37th AIAA/ASME/ASCE/AHS/ASC Structures, Structural Dynamics, and Materials Conference, Salt Lake City, Utah, April 15–17, 1996

12a. DISTRIBUTION/AVAILABILITY STATEMENT
Unclassified–Unlimited
Subject Category 39
Availability: NASA CASI (301) 621-0390

12b. DISTRIBUTION CODE

13. ABSTRACT *(Maximum 200 words)*
Results of buckling and nonlinear analyses of the Space Shuttle external tank superlightweight liquid-oxygen (LO_2) tank are presented. Modeling details and results are presented for two prelaunch loading conditions and for two full-scale structural tests that were conducted on the original external tank. The results illustrate three distinctly different types of nonlinear response for thin-walled shells subjected to combined mechanical and thermal loads. The nonlinear response phenomena consist of bifurcation-type buckling, short-wavelength nonlinear bending, and nonlinear collapse associated with a limit point. For each case, the results show that accurate predictions of nonlinear behavior generally require a large-scale, high-fidelity finite-element model. Results are also presented that show that a fluid-filled launch-vehicle shell can be highly sensitive to initial geometric imperfections. In addition, results presented for two full-scale structural tests of the original standard-weight external tank suggest that the finite-element modeling approach used in the present study is sufficient for representing the nonlinear behavior of the superlightweight LO_2 tank.

14. SUBJECT TERMS
Space Shuttle external tank; Nonlinear stability analysis; Launch vehicles; Buckling

15. NUMBER OF PAGES
27

16. PRICE CODE
A03

17. SECURITY CLASSIFICATION OF REPORT	18. SECURITY CLASSIFICATION OF THIS PAGE	19. SECURITY CLASSIFICATION OF ABSTRACT	20. LIMITATION OF ABSTRACT
Unclassified	Unclassified	Unclassified	